

# Superradiant instabilities in astrophysical systems

Helvi Witek,<sup>1,2,\*</sup> Vitor Cardoso,<sup>1,3</sup> Akihiro Ishibashi,<sup>4</sup> and Ulrich Sperhake<sup>1,2,5,6</sup>

<sup>1</sup>*CENTRA, Departamento de Física, Instituto Superior Técnico,  
Universidade Técnica de Lisboa - UTL, Avenida Rovisco Pais 1, 1049 Lisboa, Portugal.*

<sup>2</sup>*Department of Applied Mathematics and Theoretical Physics, Centre for Mathematical Sciences,  
University of Cambridge, Wilberforce Road, Cambridge CB3 0WA, UK*

<sup>3</sup>*Department of Physics and Astronomy, The University of Mississippi, University, MS 38677, USA.*

<sup>4</sup>*Department of Physics, Kinki University, Higashi-Osaka 577-8502, Japan*

<sup>5</sup>*Institute of Space Sciences, CSIC-IEEC, 08193 Bellaterra, Spain*

<sup>6</sup>*California Institute of Technology, Pasadena, CA 91125, USA*

(Dated: February 20, 2013)

Light bosonic degrees of freedom have become a serious candidate for dark matter, which seems to pervade our entire universe. The evolution of these fields around curved spacetimes is poorly understood but is expected to display interesting effects. In particular, the interaction of light bosonic fields with supermassive black holes, key players in most galaxies, could provide colourful examples of superradiance and nonlinear bosonova-like collapse. In turn, the observation of spinning black holes is expected to impose stringent bounds on the mass of putative massive bosonic fields in our universe.

Our purpose here is to present a comprehensive study of the evolution of linearized massive scalar and vector fields in the vicinities of rotating black holes. The evolution of generic initial data has a very rich structure, depending on the mass of the field and of the black hole. Quasi-normal ringdown or exponential decay followed by a power-law tail at very late times is a generic feature of massless fields at intermediate times. Massive fields generically show a transition to power-law tails early on. For a certain boson field mass range, the field can become trapped in a potential barrier outside the horizon and transition to a bound state. Because there are a number of such quasi-bound states, the generic outcome is an amplitude modulated sinusoidal, or beating, signal, whose envelope is well described by the two lowest overtones. We believe that the appearance of such beatings has gone unnoticed in the past, and in fact mistaken for exponential growth. The amplitude modulation of the signal depends strongly on the relative excitation of the overtones, which in turn is strongly tied to the bound-state geography.

A fine tuning of the initial data allows one to see the evolution of the nearly pure bound state mode which turns unstable for sufficiently large black hole rotation. For the first time we explore massive vector fields in generic BH background which are hard, if not impossible, to separate in the Kerr background. Our results show that spinning BHs are generically strongly unstable against massive vector fields.

PACS numbers: 98.80.Es, 11.25.Wx, 14.80.Va, 04.70.-s

---

\* h.witek@damtp.cam.ac.uk

# CONTENTS

I. Introduction	2
II. Setup: action, equations of motion and background metric	5
A. Action and equations of motion	5
B. Background in horizon penetrating coordinates	7
C. Initial data	8
D. Wave extraction and output	9
E. Numerical implementation	9
III. Scalar field evolutions	10
A. A summary of results in the literature	10
B. Space dependent mass coupling and massless scalars	11
C. Massive scalar fields	12
1. Bound states	13
2. Damped states: ringdown and tails	13
3. Massive scalar fields: mode excitation and beating	15
IV. Proca field evolutions	17
A. Massless vector fields	18
B. Proca field in Schwarzschild backgrounds and in the slow-rotating limit	19
C. Instability of Proca fields in highly spinning Kerr backgrounds	21
V. Conclusions	22
VI. Acknowledgements	24
A. Flux formula	25
B. Spin-weighted spherical harmonics	27
References	28

## I. INTRODUCTION

One of the most exciting outcomes of General Relativity (GR) are black holes (BHs), the physics of which has grown into a mature and fully developed branch of GR and extensions thereof [1, 2]. Observations of, e.g., X-ray binaries indicate that solar mass ( $3 - 30M_{\odot}$ ) BHs mark the endpoint of the life of massive stars and are anticipated to be a significant component of the galaxies' population. Supermassive BHs (SMBHs) with masses  $10^6 - 10^9 M_{\odot}$  or higher are conjectured to be hosted in the center of most galaxies, controlling galaxy growth and evolution, stellar birth and powering active galactic nuclei and other powerful phenomena.

Tremendous progress has been made in actually observing some of the fascinating general relativistic effects. From X-ray spectra on the inner edge of accretion disks, which probe the innermost stable circular orbit of the geometry, to gravitational wave (GW) physics, “precision BH physics” is a new and rapidly developing field [3–5]. The future holds the promise to observe some of these effects accurately by monitoring the supermassive BH at the center of our own galaxy.

One of the fundamental reasons why precision BH physics is possible at all, are the no-hair and uniqueness theorems: BHs in 4-dimensional, asymptotically flat spacetimes must belong to the Kerr-Newman family and are, thus, fully specified by three parameters only: their mass, angular momentum and electric charge (see e.g. Ref. [6, 7], or Carter's contribution to Ref. [8]). In more colloquial terms, this is commonly expressed by saying that BHs have no hair or, rather, have three hairs only. This simple yet powerful result has far reaching consequences: Given some arbitrary perturbations with the same conserved charges, they must all decay to the same final state, namely one BH with those charges. By now, there are a plethora of studies, at the perturbative and fully non-linear level, investigating how this unique final state is approached (see, e.g., Ref. [9, 10] for recent overviews). In the following we briefly summarize these studies.

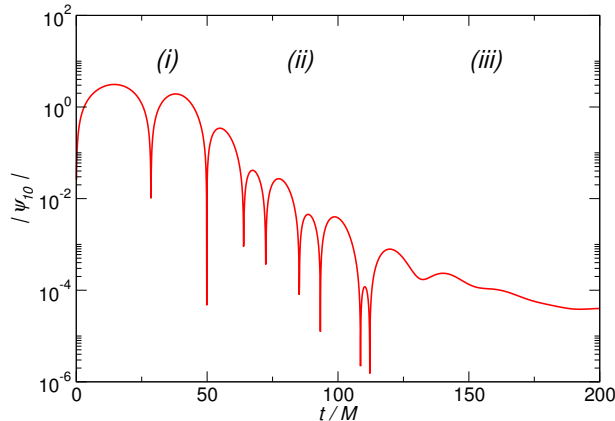


FIG. 1. Time evolution of a dipole ( $l = 1, m = 0$ ) scalar Gaussian wave packet in Schwarzschild background. We clearly observe the main features of such a field: (i) a prompt response at early times followed by (ii) the quasi-normal mode ringdown and (iii) a late-time tail.

**Generic response of a BH spacetime to external perturbations.** The generic behavior of massless fields around a BH is illustrated in Fig. 1, where we plot the evolution of a Gaussian wave packet  $\Psi = e^{-(r-10)^2/10^2}$  around a Schwarzschild BH. The particular initial data refers to a scalar field, but the qualitative results are universal and independent of the initial conditions. The generic behavior of massless fields around a BH can be divided into three parts (c.f. Fig. 1):

- (i) An initial data-dependent prompt response at early times, which is the counterpart to light-cone propagation in flat space;
- (ii) An exponentially decaying “ringdown” phase at intermediate times, where the BH is ringing with its characteristic quasi-normal modes (QNMs). This stage typically dominates the signal, and its properties, such as vibration frequency and decay timescale, depend solely on the parameters of the *final* BH [9]. Because of the no-hair theorem, the detection of QNMs allows one to uniquely determine the BH mass and spin and provides tests of GR [9, 11, 12];
- (iii) At late times, the signal is dominated by a power-law fall-off, known as “late-time tail” [13–15]. Tails are caused by backscattering off spacetime curvature and more generically by a failure of Huygen’s principle. As such, tails also appear in other situations where light propagation is not *on* the light cone such as in massive field propagation in Minkowski spacetime [16], or massless field propagation in odd-dimensional spacetimes [17].

**Superradiant effects.** The long-lasting oscillation of the lowest QNMs is the most important stage in the life of any field around a BH. Its lifetime, or quality factor, depends solely on the BH spin [9]. Specifically, the lifetime tends to increase with growing spin and the decay timescale approaches zero for nearly extremal BHs. This behaviour is tightly connected to *superradiance* [18–20]: In a scattering experiment of low-frequency waves off a BH the scattered wave is amplified if the real part of its frequency  $\omega_R$  satisfies the superradiant condition

$$\omega_R < m\Omega_H, \quad (1)$$

where  $m$  is the azimuthal “quantum” number and  $\Omega_H$  is the angular velocity of the BH horizon. We refer the reader to App. A for a derivation of this condition for both, scalar and vector fields. The excess energy is withdrawn from the object’s rotational energy [18, 19] and, in a dynamical scenario, the BH would presumably spin down. The effect can be attributed to the existence of negative-energy states in the ergo-region, and dissipation at the event horizon.

Superradiance is the chief cause of a number of exciting phenomena in BH physics:

- (i) Generic perturbations are damped away to infinity and across the event horizon. Because rotating BHs amplify waves that fulfill the superradiant condition, Eq. (1), the amplification factors as well as the quality factor of these superradiant modes increase with rotation.
- (ii) Satellites around BHs typically spiral inwards as time goes by, due to gravitational wave emission and energy conservation. Emission of radiation to infinity results in a larger binding energy of the particle. Because superradiance implies the extraction of the BH’s rotational energy, it is possible that the energy deficit comes entirely from the BH kinetic energy. In this way, satellites around rapidly spinning BHs can *in principle* orbit at a nearly fixed radius –

on so-called floating orbits – for a much longer time, tapping the BH’s kinetic energy. In BH binaries, this effect can dominate in the presence of resonances [21–23]. This phenomenon is analogous to tidal acceleration, e.g., in case of the Earth-moon system [24, 25].

(iii) A further interesting effect can be triggered by enclosing the spinning BH inside a perfectly reflecting cavity. As was recognized already by Zel’dovich [18, 19], any initial perturbation will get successively amplified near the BH and reflected back at the mirror, thus creating an instability, which was termed the “BH bomb” [26, 27]. Whereas the setup appears physically artificial at first glance, the role of the mirror can actually be realized naturally in many ways, including an anti-de Sitter spatial infinity. In this case, the BH bomb translates into a real, physical instability of (small) rotating BHs in asymptotically AdS spacetimes [28–31].

(iv) Finally, of direct interest for the present study is the fact that massive fields around Kerr BHs are also prone to a BH bomb-like instability, because the mass term effectively confines the field [32–39].

Consider a scalar field surrounding a black hole with mass  $M$  and angular momentum  $J = aM$ . The instability is regulated by the dimensionless parameter  $\mu_S M$  (from now on we set  $G = c = 1$ ), where  $m_s = \mu_S \hbar$  is the scalar field mass, and is described by the time dependence of the field,  $\Psi \sim e^{-i\omega t}$  with complex frequency  $\omega = \omega_R + i\omega_I$ . For small coupling  $M\mu_S \ll 1$  the characteristic (unstable mode) frequency giving rise to the instability is [40, 41]<sup>1</sup>

$$M\omega_I = \frac{a}{48M} (M\mu_S)^9. \quad (2)$$

In the opposite limit, i.e., for very large mass couplings  $M\mu_S \gg 1$ , the characteristic inverse time is [33]

$$M\omega_I = 10^{-7} \exp(-1.84M\mu_S). \quad (3)$$

The instability timescales are typically large. The scalar field growth rate has a global maximum of  $\tau \equiv 1/\omega_I \sim 10^7 M$  for the dipole with mass coupling  $M\mu_S = 0.42$  in the background of a Kerr BH with  $a/M = 0.99$  [36, 37].

The above results refer to massive scalar fields in the background of Kerr BHs. It was widely believed that massive vectors would be subject to a similar instability. Unfortunately, the non-separability of the field equations renders this a non-trivial problem. Recently, significant progress has been made, with a thorough study of massive vector fields around Schwarzschild BHs [42] and slowly rotating Kerr BH backgrounds [40, 41]. Pani *et al* use a slow-rotation expansion of the Fourier transformed field equations, accurate to second order in rotation, to prove that the Kerr spacetime is indeed unstable against massive vector fields [40, 41]. The massive vector field instability can be orders of magnitude stronger (i.e., shorter timescales) than its scalar counterpart.

All these calculations have been performed in the linear regime, thus neglecting backreaction effects such as the BH spin-down or effects due to non-linear self-interaction of the scalar field. Therefore, the final state of the superradiant instability in the fully dynamical regime is not known, partly because it requires the non-linear evolution of Einstein’s equations for a timescale of order  $10^6 M$ . A plausible evolution scenario consists of an exponentially growing scalar condensate outside the BH, extracting energy and angular momentum from the BH until the superradiant extraction stops, i.e., until the condition (1) is no longer satisfied. Further interesting new phenomena arise when we consider non-linear interaction terms, such as bosonova-type collapse presented in Refs. [43–45], or higher dimensional background spacetimes, such as the boosted black string recently reported in [46] or the Schwarzschild-Tangherlini solution discussed in [47, 48].

**Superradiant instability in astrophysical systems.** Massive fields in the vicinity of BHs are subject to a BH bomb-like, superradiant instability, and they grow exponentially with time. However, the effect is very weak for known standard model particles in astrophysical environments: For example, the mass coupling for the lightest known elementary scalar particle, the pion, around a solar mass BH is  $M\mu_S \sim 10^{18}$ , resulting in an instability timescale much larger than the age of the universe. Nevertheless, the superradiant instability might become significant if we consider standard model particles around primordial BHs (see, e.g., [49, 50]) or if there exist fields with small, but non-vanishing mass. One exciting possibility for these fields is provided by axions, ultralight bosonic states emerging from string-theory compactifications, which have not been ruled out by current experiments. In the “axiverse” scenario an entire landscape of ultra-light pseudo-scalar fields covering a mass range from  $10^{-33} \text{eV} \leq \mu_S \leq 10^{-8} \text{eV}$  has been proposed (see [3, 4, 43] for recent overviews). In fact, the existence of ultra-light axions leads to a plethora of possible observational implications and signatures, such as modifications of the cosmic-microwave background polarization (for  $10^{-33} \text{eV} \leq \mu_S \leq 10^{-28} \text{eV}$ ). They are also anticipated to make up a fraction of dark matter if  $10^{-28} \text{eV} \leq \mu_S \leq 10^{-22} \text{eV}$  [3, 51, 52]. Of particular interest in the context of BH physics are axions in the mass range  $10^{-22} \text{eV} \leq \mu_S \leq 10^{-10} \text{eV}$  [3, 4, 43]. Then, the time scales for the superradiant instability become astrophysically significant, giving rise to a number of interesting effects:

<sup>1</sup> Notice the difference of a factor 2 to the original result [34].

- (i) A bosonic cloud bounded in the vicinity of a Kerr BH might create a “gravitational atom”, which can be de-excited by the emission of gravitons, thus carrying away BH angular momentum;
- (ii) If the accretion of bosons from this cloud is efficient enough, the rotation of the BH can be sustained and it might be turned into a GW pulsar;
- (iii) If, on the other hand, the accretion from the axionic cloud is not efficient enough, the BH will eventually spin down, thus yielding gaps in the Regge plane (the phase-space spanned by mass and spin parameter of the BH). Further possible effects have been discussed in Refs. [3, 4, 21, 22, 43–45, 53].

Similar superradiant instabilities are expected to occur for massive hidden  $U(1)$  vector fields, which are also a generic feature of extensions of the standard model [54–57]. As already stated, while superradiant instabilities have been widely studied for massive scalar fields [21, 26, 27, 32, 36, 37, 58, 59], the case of massive vector fields is still in its infancy, though significant work along these lines was recently reported [40–42, 47, 48].

So far most studies on the massive boson instability have been performed in Fourier space. An early attempt at studying the massive scalar field instability in the time domain, with generic initial conditions was presented by Strafuss and Khanna [60]. We believe that, while the technical study may be correct, some of its conclusions are not; specifically, the authors reported an instability growth rate of  $M\omega_I \sim 2 \cdot 10^{-5}$ , which is two orders of magnitude larger than previous results in the frequency domain [36, 37] and more recent numerical studies in the time domain [44, 61]. We will attempt a correct explanation for these puzzling results in the body of this work.

The purpose of the present study is to investigate the time evolution of generic linearized massive scalar and vector fields in the vicinities of spinning BHs. Surprisingly, not much seems to have been done on this problem. Our “generic” initial data consists of Gaussian wave packets, but we will also study the evolution of bound state modes. The exploration of nonlinear gravitational dynamics or self-interactions will be presented elsewhere.

This work is organized as follows: In Sec. II we present the numerical framework, describing the formulation as a Cauchy problem, the setup of initial configurations and the background spacetime. Sec. III is devoted to the numerical results of massive scalar field evolution. In particular, we present a number of benchmark tests to verify our implementation before studying more generic setups. We will show that the evolution of a massive scalar has a non-trivial pattern, which can be explained in terms of multi-mode excitation. We believe that this pattern also describes the results reported by Strafuss and Khanna [60]. In Sec. IV we discuss our investigations of the massive vector (also known as Proca [57]) field in generic Kerr BH backgrounds, where we show, for the first time in a time evolution of rapidly spinning BHs, that Kerr BHs are strongly unstable against these fields. Finally, we summarize our results and present concluding remarks in Sec. V.

## II. SETUP: ACTION, EQUATIONS OF MOTION AND BACKGROUND METRIC

### A. Action and equations of motion

We consider a generic action [3, 62] involving one complex, massive scalar  $\Psi$  and a massive vector field  $A_\mu$  with mass  $m_S = \mu_S \hbar$  and  $m_V = \mu_V \hbar$ , respectively,

$$S = \int d^4x \sqrt{-g} \left( \frac{R}{k} - \frac{1}{4} F^{\mu\nu} F_{\mu\nu} - \frac{\mu_V^2}{2} A_\nu A^\nu - \frac{k_{\text{axion}}}{2} \Psi^* F^{\mu\nu} F_{\mu\nu} - \frac{1}{2} g^{\mu\nu} \Psi_{,\mu}^* \Psi_{,\nu} - \frac{\mu_S^2}{2} \Psi^* \Psi - V(\Psi) \right). \quad (4)$$

Here, the potential  $V(\Psi)$  is of cubic or higher order in the scalar field. The scalar and vector fields are allowed to interact through the axion-like coupling constant  $k_{\text{axion}}$ .  $F_{\mu\nu} \equiv \nabla_\mu A_\nu - \nabla_\nu A_\mu$  is the Maxwell tensor and  $*F^{\mu\nu} \equiv \frac{1}{2} \epsilon^{\mu\nu\rho\sigma} F_{\rho\sigma}$  is its dual. Here,  $\epsilon^{\mu\nu\rho\sigma} \equiv \frac{1}{\sqrt{-g}} E^{\mu\nu\rho\sigma}$  and  $E^{\mu\nu\rho\sigma}$  is the totally anti-symmetric Levi-Civita symbol with  $E^{0123} = 1$ .<sup>2</sup> The resulting equations of motion are

$$(\nabla_\nu \nabla^\nu - \mu_S^2) \Psi = \frac{k_{\text{axion}}}{2} *F^{\mu\nu} F_{\mu\nu} + V'(\Psi), \quad (5a)$$

$$\nabla_\nu F^{\mu\nu} + \mu_V^2 A^\mu = -2k_{\text{axion}} *F^{\mu\nu} \partial_\nu \Psi, \quad (5b)$$

$$\begin{aligned} \frac{1}{k} \left( R^{\mu\nu} - \frac{1}{2} g^{\mu\nu} R \right) = & -\frac{1}{8} F^{\alpha\beta} F_{\alpha\beta} g^{\mu\nu} + \frac{1}{2} F_\alpha^\mu F^{\nu\alpha} - \frac{1}{4} \mu_V^2 A_\alpha A^\alpha g^{\mu\nu} + \frac{\mu_V^2}{2} A^\mu A^\nu \\ & - \frac{1}{2} g^{\mu\nu} \left( \frac{1}{2} \Psi_{,\alpha}^* \Psi^{,\alpha} + \frac{\mu_S^2}{2} \Psi^* \Psi + V(\Psi) \right) + \frac{1}{4} (\Psi^{*,\mu} \Psi^{,\nu} + \Psi^{,\mu} \Psi^{*,\nu}). \end{aligned} \quad (5c)$$

<sup>2</sup> The identity  $\nabla_\nu *F^{\mu\nu} = 0$  is useful to derive the equations of motion for the Chern-Simons term.

We note that these equations describe the fully non-linear evolution of the system. Also, we have written the equations such that all terms quadratic or of higher order in the vector or scalar fields appear on the right hand side. In the remainder of this work, we will restrict ourselves to the case of scalar and vector fields with small amplitudes and will ignore the higher-order contributions on the right-hand sides of (5a)-(5c).

Under this assumption Eq. (5c) is equivalent to Einstein's equations in vacuum and a solution to this equation is the Kerr metric which in Boyer-Lindquist coordinates is given by

$$ds^2 = - \left(1 - \frac{2Mr_{\text{BL}}}{\Sigma}\right) dt^2 + \left(1 + \frac{2Mr_{\text{BL}}}{\Sigma}\right) dr_{\text{BL}}^2 + \Sigma d\theta^2 + \sin^2 \theta \left(r_{\text{BL}}^2 + a^2 + \frac{2Ma^2 r_{\text{BL}} \sin^2 \theta}{\Sigma}\right) d\phi^2 \\ + \left(\frac{4Mr_{\text{BL}}}{\Sigma}\right) dt dr_{\text{BL}} - \left(\frac{4Mr_{\text{BL}} a \sin^2 \theta}{\Sigma}\right) dt d\phi - 2a \sin^2 \theta \left(1 + \frac{2Mr_{\text{BL}}}{\Sigma}\right) dr_{\text{BL}} d\phi, \quad (6)$$

with

$$\Sigma = r_{\text{BL}}^2 + a^2 \cos^2 \theta, \quad \Delta = r_{\text{BL}}^2 - 2Mr_{\text{BL}} + a^2. \quad (7)$$

This geometry describes a rotating BH with mass  $M$  and angular momentum  $J = aM$ . Note that in order to ensure the regularity of the spacetime, i.e. the existence of an event horizon, the BH spin is constrained by the Kerr bound  $a/M \leq 1$ .

A second consequence of our assumptions is that the axionic coupling can be neglected. This means that we effectively study minimally coupled massive scalar and vector fields separately and our results will describe small linearized fields around the Kerr background. Any potential instability we find is consistent with the above assumptions for timescales small enough such that the fields are small. Over long timescales, the fields may grow to large amplitudes where our assumption no longer remains valid and a non-linear study becomes necessary. We postpone such non-linear evolutions to a future investigation.

In our approximation, the scalar and vector field dynamics are governed by the linearized version of Eqs. (5a) and (5b)

$$(\nabla_\nu \nabla^\nu - \mu_S^2) \Psi = 0, \quad (8a)$$

$$\nabla_\nu F^{\mu\nu} + \mu_V^2 A^\mu = 0, \quad (8b)$$

while the Kerr metric (6) satisfies  $G_{\mu\nu} = 0$ , i. e. Eq. (5c) linearized in  $\Psi$  and  $A_\mu$ .

**Evolution equations for scalar fields.** Because we intend to solve the equations of motion (8a) and (8b) numerically, it is convenient to reformulate them as time evolution problem. For this purpose we employ the 3 + 1-decomposition of the spacetime (see e.g. [63]) and consider the background spacetime in generic 3 + 1-form

$$ds^2 = -\alpha^2 dt^2 + \gamma_{ij}(dx^i + \beta^i dt)(dx^j + \beta^j dt). \quad (9)$$

Here,  $\gamma_{ij}$  is the spatial metric and  $\alpha$  and  $\beta^i$  are the lapse function and shift vector which represent the coordinate or gauge freedom of general relativity. We introduce the conjugated momenta

$$\Pi_R = -\frac{1}{\alpha}(\partial_t - \mathcal{L}_\beta)\Psi_R, \quad \Pi_I = -\frac{1}{\alpha}(\partial_t - \mathcal{L}_\beta)\Psi_I, \quad (10)$$

where  $X_R := \Re(X)$  and  $X_I := \Im(X)$  denote the real and imaginary parts, respectively. Definition (10) provides evolution equations for the scalar field  $\Psi$

$$\partial_t \Psi_R = \mathcal{L}_\beta \Psi_R - \alpha \Pi_R, \quad \partial_t \Psi_I = \mathcal{L}_\beta \Psi_I - \alpha \Pi_I, \quad (11)$$

where  $\mathcal{L}_\beta \Psi_{R,I} = \beta^k \partial_k \Psi_{R,I}$ . By applying the 3 + 1-split to the Klein-Gordon equation (8a), we obtain the evolution equations for the momentum

$$\partial_t \Pi_R = \mathcal{L}_\beta \Pi_R - D^i \alpha D_i \Psi_R + \alpha(-D^i D_i \Psi_R + K \Pi_R + \mu_S^2 \Psi_R) \quad (12a)$$

$$\partial_t \Pi_I = \mathcal{L}_\beta \Pi_I - D^i \alpha D_i \Psi_I + \alpha(-D^i D_i \Psi_I + K \Pi_I + \mu_S^2 \Psi_I), \quad (12b)$$

where  $\mathcal{L}_\beta \Pi_{R,I} = \beta^k \partial_k \Pi_{R,I}$ .  $D_i$  is the covariant derivative associated with the 3-metric  $\gamma_{ij}$  and  $K$  is the trace of the extrinsic curvature.

**Evolution equations for vector fields.** We next apply the 3+1 decomposition to the evolution equation (8b) and obtain

$$\nabla^\nu \nabla_\mu A_\nu - \nabla^\nu \nabla_\nu A_\mu + \mu_V^2 A_\mu = - [\nabla^\nu \nabla_\nu A_\mu - \nabla_\mu (\nabla^\nu A_\nu) - R_\mu{}^\nu A_\nu - \mu_V^2 A_\mu] = 0. \quad (13)$$

By operating with  $\nabla^\mu$  on Eq. (13) it is straight-forward to show that the Lorenz gauge

$$\nabla^\mu A_\mu = 0 \quad (14)$$

needs to be satisfied. For a vacuum background spacetime as considered in our work, we also have  $R_{\mu\nu} = 0$  and Eq. (13) simplifies to

$$\nabla^\nu \nabla_\nu A_\mu - \mu_V^2 A_\mu = 0. \quad (15)$$

Note, that in case of a non-vanishing cosmological constant  $\Lambda$ ,  $R_{\mu\nu} = \Lambda g_{\mu\nu}$  and in place of Eq. (15) we would obtain

$$\nabla^\nu \nabla_\nu A_\mu - (\Lambda + \mu_V^2) A_\mu = 0, \quad (16)$$

i. e. the cosmological constant enters as an additional “mass”-like term. In particular, it changes the evolution equation of a massless vector field to that of a massive one. Note, however, that the Maxwell equations in Kerr-(anti-)de Sitter background are known to be separable and can be written in the form of a Teukolsky type equation [29, 64, 65]. Therefore, one might expect that the equations of motion for a massive vector field in a vacuum Kerr spacetime should also be separable. We emphasize, however, that this analogy between a massless field with cosmological constant and a massive one without needs to be taken with care: a massless vector field has only 2 dynamical degrees of freedom irrespective of the value of the cosmological constant, whereas a massive vector field has 3. In fact, up to date, a separation of the equations of motion for a massive vector field has not been accomplished. It is not immediately obvious, for this reason, whether there exists a well-defined correspondence between the two cases. In this work we focus on  $\Lambda = 0$  and therefore leave a detailed investigation of this question for future work.

We now apply the 3+1 decomposition to the vector field and split  $A_\mu$  into its spatial part and normal component

$$\mathcal{A}_\mu = \gamma^\nu{}_\mu A_\nu, \quad \text{and} \quad \varphi = -n^\mu A_\mu, \quad (17)$$

where  $n^\mu$  is the vector normal to the spatial hypersurface  $\Sigma$ . The vector field can be reconstructed from its projections according to  $A_\mu = \mathcal{A}_\mu + n_\mu \varphi$ . Furthermore, the projection of the Maxwell tensor along the normal vector  $n^\mu$  yields the electric field

$$E_\mu = F_{\mu\nu} n^\nu, \quad (18)$$

which is a purely spatial quantity, i.e.,  $E_\mu n^\mu = 0$ .

With all the necessary ingredients at hand we now proceed by performing the 3 + 1-split Eqs. (14) and (15). In terms of the dynamical variables  $\{\varphi, \mathcal{A}_i, E_i\}$  this procedure results in the constraint

$$C_E = D^i E_i + \mu_V^2 \varphi = 0. \quad (19)$$

and in the evolution equations

$$(\partial_t - \mathcal{L}_\beta) \varphi = -\alpha (D^i \mathcal{A}_i - K \varphi) - \mathcal{A}_i D^i \alpha, \quad (20a)$$

$$(\partial_t - \mathcal{L}_\beta) \mathcal{A}_i = -\alpha (E_i + D_i \varphi) - \varphi D_i \alpha, \quad (20b)$$

$$(\partial_t - \mathcal{L}_\beta) E_i = \alpha (\mu_V^2 \mathcal{A}_i + K E_i - 2E^j K_{ij} + D^j (D_i \mathcal{A}_j - D_j \mathcal{A}_i)) + D^j \alpha (D_i \mathcal{A}_j - D_j \mathcal{A}_i), \quad (20c)$$

where  $\mathcal{L}_\beta \varphi = \beta^k \partial_k \varphi$ ,  $\mathcal{L}_\beta \mathcal{A}_i = \beta^k \partial_k \mathcal{A}_i + \mathcal{A}_k \partial_i \beta^k$  and  $\mathcal{L}_\beta E_i = \beta^k \partial_k E_i + E_k \partial_i \beta^k$ .

## B. Background in horizon penetrating coordinates

In practice, it is convenient to employ horizon penetrating coordinates and consider the Kerr spacetime in Cartesian Kerr-Schild coordinates  $(t, x, y, z)$ . Without loss of generality, we assume the angular momentum to point in the  $z$  direction. Then, the Kerr-Schild form of the lapse function  $\alpha$ , shift vector  $\beta^i$ , 3-metric  $\gamma_{ij}$  and extrinsic curvature  $K_{ij}$  is given by

$$\alpha = (1 + 2Hl^t l^t)^{-1/2}, \quad \beta^i = -\frac{2Hl^t l^i}{1 + 2Hl^t l^t}, \quad \gamma_{ij} = \delta_{ij} + 2Hl_i l_j, \quad (21a)$$

$$K_{ij} = -\frac{1}{\alpha} (l_i l_j \partial_t H + 2Hl_{(i} \partial_t l_{j)}) - 2\alpha (\partial_{(i} (l_{j)} H l^t) + 2H^2 l^t l^k l_{(i} \partial_{|k|} l_{j)} + Hl^t l_i l_j l^k \partial_k H), \quad (21b)$$

where

$$H = \frac{Mr_{\text{BL}}^3}{r_{\text{BL}}^4 + a^2 z^2}, \quad l_\mu = \left( 1, \frac{r_{\text{BL}}x + ay}{r_{\text{BL}}^2 + a^2}, \frac{r_{\text{BL}}y - ax}{r_{\text{BL}}^2 + a^2}, \frac{z}{r_{\text{BL}}} \right). \quad (22)$$

and the Boyer-Lindquist radial coordinate  $r_{\text{BL}}$  is related to the Cartesian Kerr-Schild coordinates by

$$\frac{x^2 + y^2}{r_{\text{BL}}^2 + a^2} + \frac{z^2}{r_{\text{BL}}^2} = 1. \quad (23)$$

### C. Initial data

In this work we consider two types of initial configurations: (i) generic pulses of Gaussian shape and (ii) bound states which are particularly suitable for identifying putative instabilities. We describe each of these initial data in detail.

**Gaussian initial data.** We specify Gaussian wave packets of the form

$$\Psi(t=0) = 0, \quad \Pi(t=0) = \exp\left(-\frac{(r-r_0)^2}{w^2}\right) {}_0\Sigma(\theta, \phi), \quad (24a)$$

$$\varphi(t=0) = 0, \quad \mathcal{A}_i(t=0) = \exp\left(-\frac{(r-r_0)^2}{w^2}\right) {}_{-1}\Sigma(\theta, \phi), \quad E_i(t=0) = 0, \quad i = 1, 2, 3, \quad (24b)$$

where  $r = \sqrt{x^2 + y^2 + z^2}$  is the Kerr-Schild radial coordinate.  $r_0$  and  $w$  are the center and width of the Gaussian, while  ${}_0\Sigma(\theta, \phi)$  and  ${}_{-1}\Sigma(\theta, \phi)$  represent superpositions of spherical harmonics  ${}_sY_{lm}(\theta, \phi)$  of spin weight  $s = 0$  and  $s = -1$ , respectively. Expressed in Cartesian coordinates  $(x, y, z)$

$$x = r \sin \theta \cos \phi, \quad y = r \sin \theta \sin \phi, \quad z = r \cos \theta, \quad (25)$$

the spin-weighted spherical harmonics up to  $l = 2$  are given by Eqs. (B1)-(B6) in Appendix B.

**Bound state initial data.** Our second type of initial data is given by the quasi-bound states of massive scalar fields around BHs which represent long-lived modes of massive scalar field perturbations around Schwarzschild or Kerr BHs and have been studied extensively in the literature in the frequency domain [9, 34, 36, 37, 40, 41, 66]. Our particular interest in these modes arises from their pure nature; they represent potentially superradiant, single-frequency states. By specifying single-mode states of this type, we are able to suppress interference or beating effects of the kind discussed below for Gaussian initial data. Evolutions of such modes additionally serve as a useful test for our code [44].

There exist powerful and simple methods to construct the bound states for massive scalars, either by direct numerical integration or a continued fraction approach [9, 14, 36, 37]. Here, we adopt Leaver's continued fraction method and obtain in Boyer-Lindquist coordinates

$$\Psi_{lm} = e^{-i\omega t_{\text{BL}}} e^{-im\phi_{\text{BL}}} S_{lm}(\theta_{\text{BL}}) R_{lm}(r_{\text{BL}}). \quad (26)$$

Here,  $S_{lm}(\theta_{\text{BL}})$  are spheroidal harmonics [67] and the radial dependence is given by

$$R_{lm}(r_{\text{BL}}) = (r_{\text{BL}} - r_{\text{BL},+})^{-i\sigma} (r_{\text{BL}} - r_{\text{BL},-})^{i\sigma + \chi - 1} e^{r_{\text{BL}}q} \sum_{n=0}^{\infty} a_n \left( \frac{r_{\text{BL}} - r_{\text{BL},+}}{r_{\text{BL}} - r_{\text{BL},-}} \right)^n, \quad (27)$$

with

$$\sigma = \frac{2r_{\text{BL},+}(\omega - \omega_c)}{r_{\text{BL},+} - r_{\text{BL},-}}, \quad q = \pm \sqrt{\mu_S^2 - \omega^2}, \quad \chi = \frac{\mu_S^2 - 2\omega^2}{q}. \quad (28)$$

$r_{\text{BL},\pm} = M \pm \sqrt{M^2 - a^2}$  are the radii of the inner and outer horizon and  $\omega_c = m\Omega_H = m \frac{a}{2Mr_{\text{BL},+}}$  is the critical frequency for superradiance. All remaining terms in this expression are known in closed form and the characteristic frequency  $\omega$  can be obtained by solving a three-term recurrence relation for the coefficients  $a_n$  given by, e.g., Eqs. (35)-(48) of [37]. For our purposes, we still need to transform these results from Boyer-Lindquist to Kerr-Schild coordinates denoted in this discussion for clarity by a subscript “KS”,

$$dt_{\text{KS}} = dt_{\text{BL}} + \frac{2Mr_{\text{BL}}}{\Delta} dr_{\text{BL}}, \quad dr_{\text{KS}} = dr_{\text{BL}}, \quad d\theta_{\text{KS}} = d\theta_{\text{BL}}, \quad d\phi_{\text{KS}} = d\phi_{\text{BL}} + \frac{a}{\Delta} dr_{\text{BL}}. \quad (29)$$



Then, the bound state scalar field is given by

$$\Psi_{lm} = e^{-i\omega t_{\text{KS}}} (r_{\text{KS}} - r_{\text{KS},+})^A (r_{\text{KS}} - r_{\text{KS},-})^B \left( \frac{r_{\text{KS}} - r_{\text{KS},+}}{r_{\text{KS}} - r_{\text{KS},-}} \right)^C Y_{lm}(\theta_{\text{KS}}, \phi_{\text{KS}}) R_{lm}, \quad (30)$$

where  $A = -\frac{2i\omega M r_{\text{KS},+}}{r_{\text{KS},-} - r_{\text{KS},+}}$ ,  $B = \frac{2i\omega M r_{\text{KS},-}}{r_{\text{KS},-} - r_{\text{KS},+}}$ ,  $C = \frac{ima}{r_{\text{KS},-} - r_{\text{KS},+}}$ . Henceforth we will drop the subscript “KS” and denote the Kerr-Schild radius and angles by  $(r, \theta, \phi)$ .

The corresponding conjugated momenta  $\Pi_{lm}$  are computed from their definition, Eq. (10). Unfortunately, a simple construction of these modes exists only for scalar fields, while for vector fields a fully numerical procedure is required [36, 37, 40, 41]. Partly for this reason and partly because Gaussian initial data turn out to be adequate for the identification of superradiant instabilities we will not consider vector bound states in the remainder of this work.

#### D. Wave extraction and output

The main diagnostic quantities extracted from our simulations are the radiated scalar and vector waves. The scalar multipoles are directly obtained from interpolating the fields  $\psi$  and  $\Pi$  onto spheres of constant coordinate radius  $r = r_{\text{ex}}$  and projecting onto  $s = 0$  spherical harmonics according to

$$\Psi_{lm}(t) = \int d\Omega \Psi(t, \theta, \phi) Y_{lm}^*(\theta, \phi), \quad \Pi_{lm}(t) = \int d\Omega \Pi(t, \theta, \phi) Y_{lm}^*(\theta, \phi). \quad (31)$$

For vector fields, we construct the gauge invariant Newman Penrose scalar [68] (see also, e.g., [69–71] for recent applications in numerical simulations).

$$\Phi_2 = F_{\mu\nu} \ell^\mu \bar{m}^\nu, \quad (32)$$

where  $\ell^\mu = \frac{1}{\sqrt{2}}(n^\mu - u^\mu)$  and  $\bar{m}^\mu = \frac{1}{\sqrt{2}}(v^\mu - w^\mu)$  are vectors of a null tetrad. In practice, the vectors of the null tetrad are constructed from a Cartesian orthonormal basis  $\{u^i, v^i, w^i\}$  on the spatial hypersurface and the timelike orthonormal vector  $n^\mu$ . Together with the reconstruction of the Maxwell tensor from

$$F_{\mu\nu} = n_\mu E_\nu - n_\nu E_\mu + D_\mu \mathcal{A}_\nu - D_\nu \mathcal{A}_\mu \quad (33)$$

we can straightforwardly derive the Newman-Penrose scalar  $\Phi_2$  whose real and imaginary components are given by

$$\Phi_2^R = -\frac{1}{2} [E_i^R v^i + u^i v^j (D_i \mathcal{A}_j^R - D_j \mathcal{A}_i^R) + E_i^I w^i + u^i w^j (D_i \mathcal{A}_j^I - D_j \mathcal{A}_i^I)], \quad (34)$$

$$\Phi_2^I = \frac{1}{2} [E_i^R w^i + u^i w^j (D_i \mathcal{A}_j^R - D_j \mathcal{A}_i^R) - E_i^I v^i - u^i v^j (D_i \mathcal{A}_j^I - D_j \mathcal{A}_i^I)]. \quad (35)$$

Finally, we obtain the multipoles by projecting  $\Phi_2$  onto  $s = -1$  spin-weighted spherical harmonics

$$\Phi_{2lm}^R(t) = \int d\Omega [\Phi_2^R(t, \theta, \phi)_{-1} Y_{lm}^R(\theta, \phi) + \Phi_2^I(t, \theta, \phi)_{-1} Y_{lm}^I(\theta, \phi)], \quad (36)$$

$$\Phi_{2lm}^I(t) = \int d\Omega [\Phi_2^I(t, \theta, \phi)_{-1} Y_{lm}^R(\theta, \phi) - \Phi_2^R(t, \theta, \phi)_{-1} Y_{lm}^I(\theta, \phi)]. \quad (37)$$

#### E. Numerical implementation

We have implemented this framework as a module LIN-LEAN in the LEAN code [72], which is based on the CACTUS computational toolkit [73, 74] and the CARPET mesh refinement package [75, 76]. The evolution equations are integrated in time using the method of lines with a fourth-order Runge-Kutta scheme and fourth-order spatial discretization on all refinement levels except the innermost where we excise the black-hole singularity and use second-order accurate stencils instead. The excision is implemented by removing a “legosphere” of radius  $r_{\text{ex}} \leq 1M$  centered on the singularity [77, 78] and therefore guaranteed to be inside the event horizon for all values of  $a$ . Inside the excision region, we set all evolution variables to their flat spacetime values  $\alpha = 1$ ,  $\beta^i = 0$ ,  $\gamma_{ij} = \delta_{ij}$  and  $K_{ij} = 0$ , and extrapolate values onto the excision boundary from the exterior regular grid; see [77, 78] for more details of this procedure.

Run	$M\mu_S$	$a/M$	${}_0\Sigma(\theta, \phi)$	Grid Setup
sS_m000	0.00	0.00	$Y_{00} + Y_{10} + Y_{1-1} - Y_{11}$	$\{(384, 192, 96, 48, 24, 12, 6, 3, 1.5), h = M/100\}$
sK_m000	0.00	0.99	$Y_{00} + Y_{10} + Y_{1-1} - Y_{11}$	$\{(384, 192, 96, 48, 24, 12, 6, 3, 1.5), h = M/108\}$
sS_m001	0.10	0.00	$Y_{11}$	$\{(1024, 512, 256, 128, 64, 32, 8, 4, 2), h = M/40\}$
sS_m042	0.42	0.00	$Y_{10} + Y_{11} + Y_{20} + Y_{22}$	$\{(1536, 384, 192, 96, 48, 24, 12, 6, 3, 1.5), h = M/60\}$
sS_m100	1.00	0.00	$Y_{11}$	$\{(1024, 512, 256, 128, 64, 32, 8, 4, 2), 1/40\}$
sK_m042 <sub>c</sub>	0.42	0.99	$Y_{00} + Y_{10} + Y_{1-1} - Y_{11}$	$\{(1536, 384, 192, 96, 48, 24, 12, 6, 3, 1.5), h = M/60\}$
sK_m042 <sub>m</sub>	0.42	0.99	$Y_{11,1-1}$	$\{(1536, 384, 192, 96, 48, 24, 12, 6, 3, 1.5), h = M/72\}$
sK_m042 <sub>f</sub>	0.42	0.99	$Y_{11,1-1}$	$\{(1536, 384, 192, 96, 48, 24, 12, 6, 3, 1.5), h = M/84\}$

TABLE I. Initial setup for simulations of a scalar field with Gaussian initial data located at  $r_0 = 12 M$  and with width  $w = 2M$  in a Schwarzschild or Kerr background. We denote the mass parameter  $M\mu_S$ , the dimensionless spin parameter  $a/M$ , the modes of the initial pulse  ${}_0\Sigma(\theta, \phi)$  and the specific grid setup, measured in units of the BH mass  $M$ , following the notation of Sec. II E in [72].

$M\mu_S$	$a/M$	$M\omega_{11} (n=0)$	$M\omega_{11} (n=1)$	$M\delta_{10}$
0.00	0.00	$0.2929 - i0.09766$	$0.2645 - i0.3063$	0.0284
0.00	0.99	$0.4934 - i0.03671$	$0.4837 - i0.09880$	0.0097
0.42	0.00	$0.4075 - i0.001026$	$0.4147 - i0.0004053$	0.0072
0.42	0.99	$0.4088 + i1.504 \cdot 10^{-7}$	$0.4151 + i5.364 \cdot 10^{-8}$	0.0063
1.00	0.00	$0.9222 - i0.11842$	$0.9570 - i0.04792$	0.0348
1.00	0.99	$0.8765 - i0.18994$	$0.9515 - i0.06292$	0.075

TABLE II. Frequencies for the fundamental ( $n = 0$ ) and first overtone ( $n = 1$ ) modes of (i) the quasi-normal modes for  $M\mu_S = 0$  and (ii) the bound states for  $M\mu_S = 0.42, 1.0$  for a set of BH spins  $a/M$  obtained with the continued fraction method. The beating frequency  $\delta_{10}$  is defined as the difference of the real parts of the frequencies for  $n = 0$  and  $n = 1$ .

### III. SCALAR FIELD EVOLUTIONS

In this section we report our results obtained for the evolution of scalar fields in BH background spacetimes. For this purpose, we have evolved Gaussian wave pulses of width  $w = 2 M$  centered at  $r_0 = 12 M$  around either a non-rotating Schwarzschild BH or a rapidly spinning Kerr BH with  $a/M = 0.99$ . The set of our simulations is summarized in Table I.

As mentioned in the introduction, the resulting signal is typically composed of three stages, a transient, an exponential ringdown phase and late-time tails. Whereas we identify these stages clearly in evolutions of massless scalar fields, the massive case exhibits a richer phenomenology which we will discuss in detail further below. First, however, we summarize results from the literature and present tests of our numerical infrastructure.

#### A. A summary of results in the literature

In the following discussion, we will make frequent use of the characteristic frequencies of the two lowest (fundamental and first overtone) modes of the dipole as obtained from a linearized analysis in the frequency domain [9, 11]. These values are summarized for a set of chosen mass parameters  $\mu_S$  of the scalar field and our two choices of the rotation parameter  $a/M$  in Table II.

In the case of massless perturbations the classification of oscillation modes is relatively straightforward; there exists one family of oscillation modes, the quasi-normal modes, characterized by an integer number and the “lowest” or fundamental mode is defined as having the largest damping time. In fact, massless perturbations are generally short-lived and decay fast (on timescales of order of the BH mass) unless the BH is rotating at nearly extremal rate. In contrast, massive perturbations generally decay on larger timescales and their class of oscillation modes contains a second family with profiles concentrated near the effective potential well. These long-lived modes, referred to as “bound states” [37], are conventionally ordered by *decreasing* absolute value of the imaginary part, i. e. the fundamental oscillation mode is defined as that with the shortest damping time. This is in contrast to the usual quasinormal modes, which are conventionally ordered by increasing imaginary part. The values for the fundamental

( $n = 0$ ) and the first overtone ( $n = 1$ ) bound state mode obtained from the continued fraction method are listed in Table II together with the difference  $\delta_{10} \equiv \omega_R^{n=1} - \omega_R^{n=0}$  which will play an important role in our interpretation of the results further below.

In the regime of small mass couplings  $M\mu_S$ , one finds an analytic approximation for the oscillation frequencies of these bound states, resembling a hydrogen-like spectrum [40, 41],

$$M\omega_R = M\mu_S - \frac{(M\mu_S)^3}{2(l+n+1)^2}, \quad (38a)$$

$$M\omega_I = -\imath\delta\nu \left( \frac{M\mu_S}{l+n+1} \right)^3, \quad (38b)$$

where  $\delta\nu$  is given by Eq. (C8) of [41].

At late times, after the relaxation of the BH, power-law tails arise [13–15, 79]. Power-law tails exist both in flat and in curved spacetime and are generically caused by a failure of Huygen’s principle. In the case of flat spacetime, they can arise in massive interactions [16] or even with massless fields in odd-dimensional spacetimes due to the peculiar nature of the Green’s function [17]. Curved backgrounds give generically rise to power-law tails which are a consequence of the continued scattering of the scalar field off the background curvature. These tails have the form

$$\Psi \sim t^p \sin(\mu_S t). \quad (39)$$

For massless scalar fields, one finds one exponent  $p$  given by

$$p = -(2l + 3). \quad (40)$$

Tails of massive perturbations, however, exhibit a more complex behaviour; details depend on the mass parameter  $\mu_S$  [80–83], but their intermediate and late-time behaviour is characterized by

$$p = -(l + 3/2), \quad \text{at intermediate times}, \quad (41a)$$

$$p = -5/6, \quad \text{at very late times}. \quad (41b)$$

These exponents are loosely associated with the two timescales  $M, \mu_S$  of the problem; in particular, intermediate times refer to the window (we assume small  $M\mu_S$ )  $M\mu_S \ll t\mu_S \ll (M\mu_S)^{-2}$ .

Note, that the intermediate-time behavior is identical to the power-law behavior of massive fields in *flat* spacetime [16] whereas the late-time behavior is also affected by scattering off the spacetime curvature.

## B. Space dependent mass coupling and massless scalars

We next employ the results summarized in the previous section to test our numerical framework. For the first test, we consider the unphysical scenario of a scalar field with space-dependent mass term  $\mu_S^2 = -10M^2/r^4$  in a Schwarzschild background. This choice is motivated by the strong instability it generates and provides a unique and fast setup to test the code in a particularly violent regime. A mode analysis of the Klein-Gordon equation for this choice of  $\mu_S$  is straightforward and demonstrates the existence of at least one unstable mode with time dependence  $\Psi \sim e^{0.071565t}$ . The results obtained for the evolution of a spherical shell described by  $\Psi_{t=0} = \frac{1}{\sqrt{4\pi}} \exp\left(-\frac{(r-12)^2}{4}\right)$  are shown in Fig. 2 which shows the amplitude of the scalar field extracted at  $r_{\text{ex}} = 10 M$  as a function of time. Our numerical results are consistent with an exponential growth,  $\Psi \sim e^{0.07161t}$  in excellent agreement with the frequency calculation.

A second test for our code is provided by the evolution of massless scalar fields around BHs, a case well studied in the literature [9, 10]. For this purpose we have initialized the field by a Gaussian with  $r_0 = 12 M$  and  $w = 2 M$  and extracted the monopole and dipole at  $r_{\text{ex}} = 10$ . The results are shown in Fig. 3 for a BH background with  $a/M = 0$  and  $a/M = 0.99$ , respectively. The waveform displays the familiar features; an early transient followed by an exponentially decaying sinusoid and a power-law tail at late times. A fit to the ringdown phase of the dipole yields numerical QNM frequencies within less than 2% of the values in Table II. Likewise, we obtain a numerical power-law tail of the form  $t^p$  for the monopole, with  $p = -3.08$  for  $a/M = 0$  and  $p = -3.07$  for  $a/M = 0.99$  in good agreement with the prediction  $p = -3$  obtained from the low-frequency expansion of the wave equation underlying Eq. (40).

Additionally, we have performed a convergence analysis for the more challenging of these two cases, that of a highly rotating BH background with  $a/M = 0.99$ . This analysis provides the estimate of the numerical uncertainties  $\Delta\Psi_{11}/\Psi_{11} \leq 8\%$  for the  $l = m = 1$  mode at late times of the evolution and  $\Delta\Psi_{00}/\Psi_{00} \leq 3\%$  for  $l = m = 0$ .

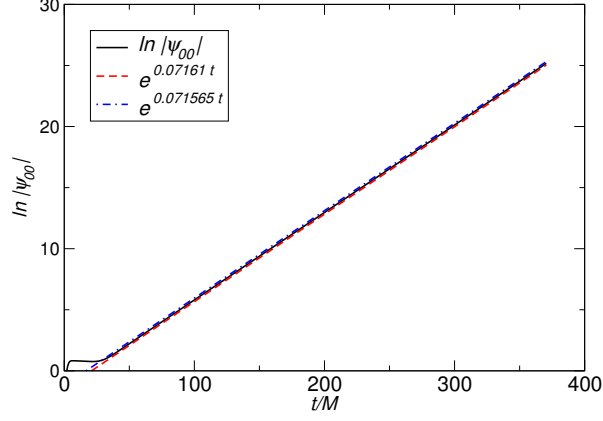


FIG. 2. Amplitude of the scalar field extracted at  $r_{\text{ex}} = 10 M$  as function of time obtained from the evolution of a scalar field initialized as spherical shell with space dependent mass  $\mu_S^2 = -10M^2/r^4$ , around a non-rotating BH.

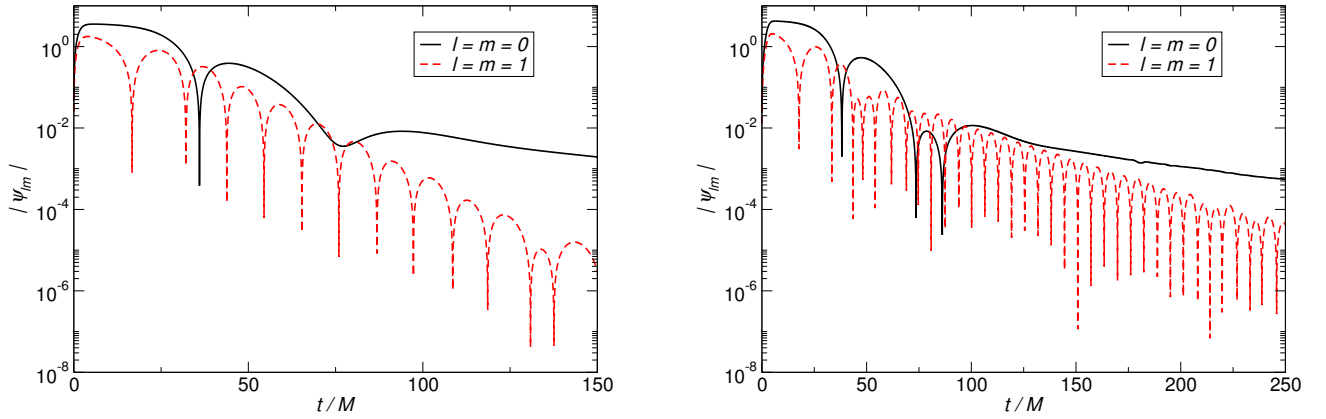


FIG. 3. Evolution of a Gaussian profile of a massless scalar field with width  $w = 2 M$  centered at  $r_0 = 12 M$  around a Schwarzschild BH (left panel) and around a Kerr BH with  $a/M = 0.99$  (right panel). We depict the  $l = 0$  (solid black line) and  $l = m = 1$  (red dashed line) multipoles.

### C. Massive scalar fields

Having tested the numerical framework, we next explore the dynamics of generic, massive scalar fields. A mass term introduces a new scale to the problem and new features appear in the evolution which depend on the particular details of the initial configuration. Roughly, these configurations can be classified into three groups.

- **Bound state configurations.** These configurations are characterized by unusually long-lived modes [21, 33–37, 44, 52, 84], and exist for any  $m, \mu_S \neq 0$ . These modes are described by Eq. (38) for small  $M\mu_S$ . If they, furthermore, satisfy the condition  $\omega_R < \mu_S \leq m\Omega_H$  they are subject to the superradiant instability.
- **Rapidly damped configurations.** Generic initial profiles of massless or massive scalar fields typically decay on short time scales via quasi-normal ringdown followed by a power-law tail.

- Beating regime. Additionally, massive fields may exhibit long-lived, strongly modulated oscillations which result from the interplay between different overtones of the same multipole.

In the following we will discuss numerical evolutions of initial configurations for each of these classes in more detail.

### 1. Bound states

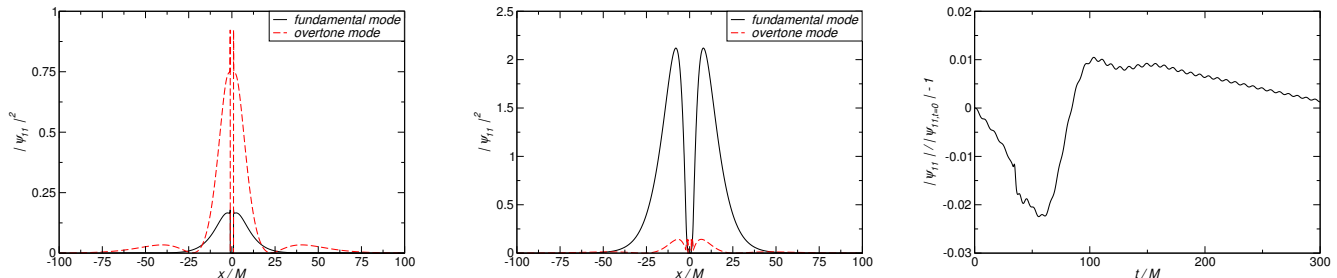


FIG. 4. Left and center: Initial profile of  $|\Psi_{11}|^2$  for a bound state  $m = 1$  dipole configuration with  $M\mu_S = 0.42$  in a Schwarzschild (left panel) and  $a/M = 0.99$  Kerr background (mid panel). Black solid lines represent the fundamental mode and red dashed lines the first overtone. Right: Relative change of the modulus of the  $(1, 1)$  mode extracted at  $r_{\text{ex}} = 20 M$ .

We have constructed bound-state initial configurations for fields with a mass coupling  $M\mu_S = 0.42$ , cf. Eq. (30), following [9, 36, 37], and evolved them in a Schwarzschild or a Kerr background with  $a/M = 0.99$ . In the left and center panels of Fig. 4 we show the modulus of the fundamental mode and first overtone of the  $m = 1$  dipole bound state along the  $x$ -axis; cf. Table II. For non-rotating BHs the fundamental bound state is localized near the origin, whereas its maxima are shifted to larger radii as the rotation parameter  $a/M$  is increased. For a highly spinning BH with  $a/M = 0.99$ , the fundamental mode is peaked at around  $r \sim 12 M$ . For the first overtone we observe a node at  $r_{\text{node}} \sim 22.5 M$  and at  $r_{\text{node}} \sim 26.5 M$  for  $a/M = 0$  and  $a/M = 0.99$ , respectively. The specific structure of the bound-state profiles will play an important role in our analysis of beating effects below.

Throughout the time evolution, we expect the bound state scalar field to remain localized in the vicinity of the BH. Thus, by construction, its absolute value  $\Psi_{11}\Psi_{11}^* \sim \exp(-i\omega t)\exp(i\omega t) \sim \text{const.}$  should remain almost constant in time, with a small growth rate of  $M\omega_I \sim 1.5 \cdot 10^{-7}$  [36, 37]. This behavior is confirmed in the animations generated from our numerical data and made available online [85]. Here we have tested these properties numerically by extracting the dipole mode as a function of time at  $r_{\text{ex}} = 20 M$ . The result is shown in the right panel of Fig. 4 for a Kerr background with  $a/M = 0.99$ . The scalar field varies by less than  $\sim 2\%$  until  $t \sim 200 M$  and by less than  $\sim 1\%$  at late times, which is within the numerical uncertainties.

We note that bound states are unstable states, but have a long instability time scale of  $\sim 10^7 M$  (see Table II), about three orders of magnitude larger than the evolution times feasible within our framework. Over the time range covered in the figure the instability has not yet generated a visible growth in amplitude.

### 2. Damped states: ringdown and tails

In order to study the behaviour of rapidly damped configurations, we initialize the field by a Gaussian wave pulse with  $r_0 = 12 M$  and  $w = 2 M$  according to Eq. (24a). The specific choices of the mass coupling  $M\mu_S$ , rotation rate  $a/M$  and the initial mode contributions for our set of simulations are summarized in Table I. The resulting dipole and monopole amplitudes for a subset of our simulations are shown in Fig. 5. For all simulations we observe the expected pattern of an early transient followed by quasi-normal ringdown and a late-time tail which is dominated by an oscillatory behaviour characterized by the mass term according to Eq. (39) and governed by scattering off spacetime curvature according to Eq. (41b) at late times [81–83].

At intermediate times we find for the case of an  $m = 1$  dipole with  $M\mu_S = 0.1$  (left upper panel of Fig. 5), an oscillatory decay of the field as  $\Psi_{11} \sim t^{-2.543} \sin(0.1t)$ , within 2% of the expected value for tails at intermediate times

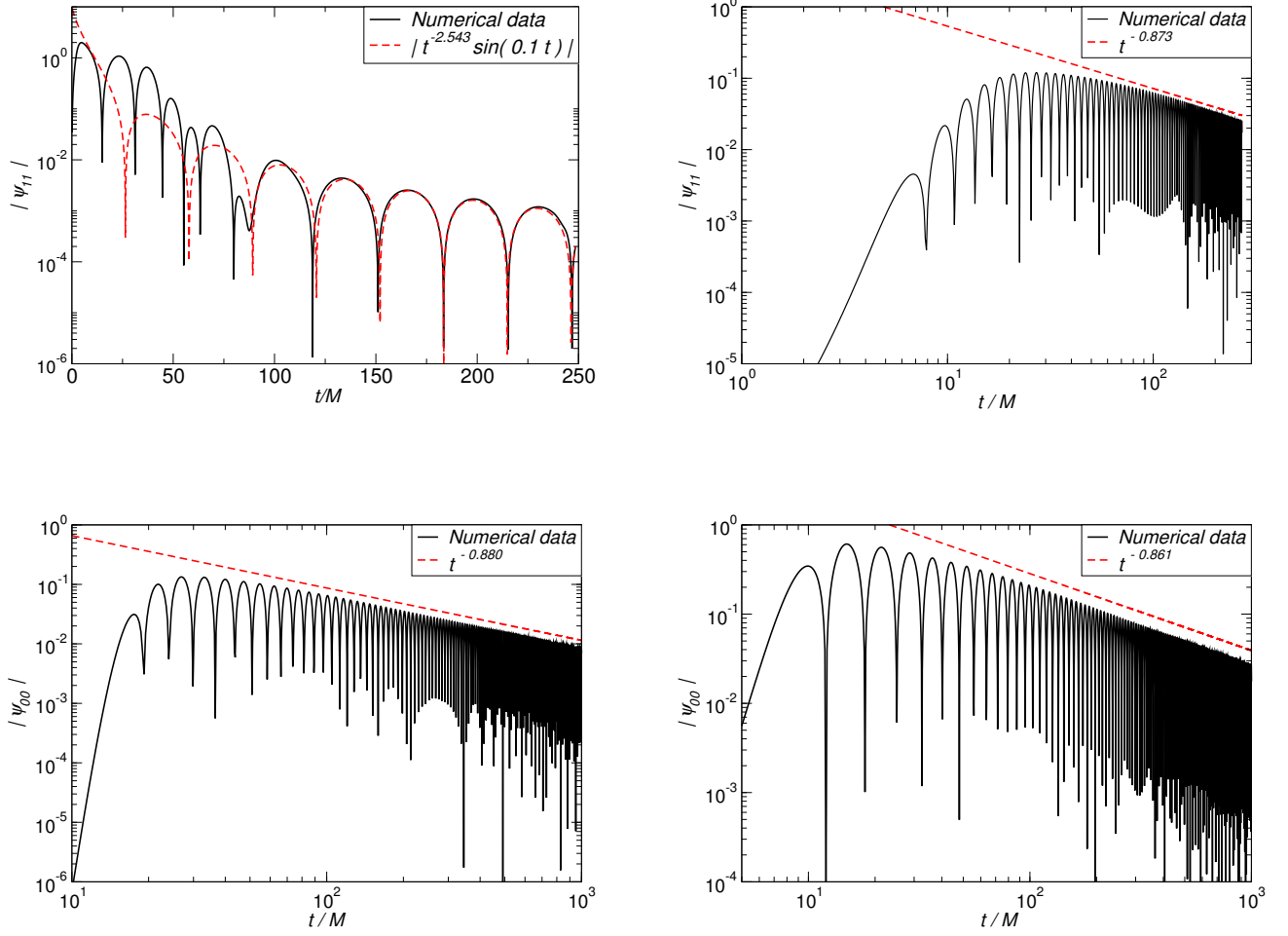


FIG. 5. Upper left:  $l = m = 1$  multipole of run sS\_m001 extracted at  $10M$ . The solid (black) line refers to numerical data, the dashed (red) to an oscillatory tail fit. Upper right: Same for sS\_m100, extracted at  $r_{\text{ex}} = 20 M$  (black solid line) together with the tail fit (red dashed line, we omit the oscillatory term for clarity). Lower Panels:  $l = m = 0$  multipole of runs sS\_m042 (left, extracted at  $20M$ ) and sK\_m042 (right, extracted at  $25M$ ). The solid black lines refer to the numerical data while the red dashed lines denote the the fit to the envelope of the oscillatory late-time tail.

[80–82]; cf. Eqs. (39) and (41a). At *very late times*, we expect a tail of the form (39) with  $p = -5/6$  to dominate, but simulation of sufficient duration are computationally too expensive with our present computational framework.

Furthermore, we consider larger mass couplings  $M\mu_S = 0.42$  and  $M\mu_S = 1$ . We present the  $l = m = 1$  dipole mode of sS\_m100 in the top right panel of Fig. 5 and the monopole modes for both runs sS\_m042 and sK\_m042 in the bottom panels of Fig. 5. Here, the intermediately-late time tail with  $p = -(l + 3/2)$  in Eq. (39) appears to be suppressed. Instead, the decay with  $p = -5/6$  expected at very late times clearly dominates the signal. Focusing on the case with mass coupling  $M\mu_S = 0.42$  we observe that the tail is present for both spinning and non-spinning BH backgrounds; cf. bottom panel of Fig. 5. For  $a/M = 0$  and  $a/M = 0.99$ , we find the exponents  $p = -0.880$  and  $p = -0.861$ , respectively, which agree within 5% with the theoretically expected late-time behaviour [81–83]. We note that these results are independent of the extraction radii  $r_{\text{ex}}$  at which the field is observed.

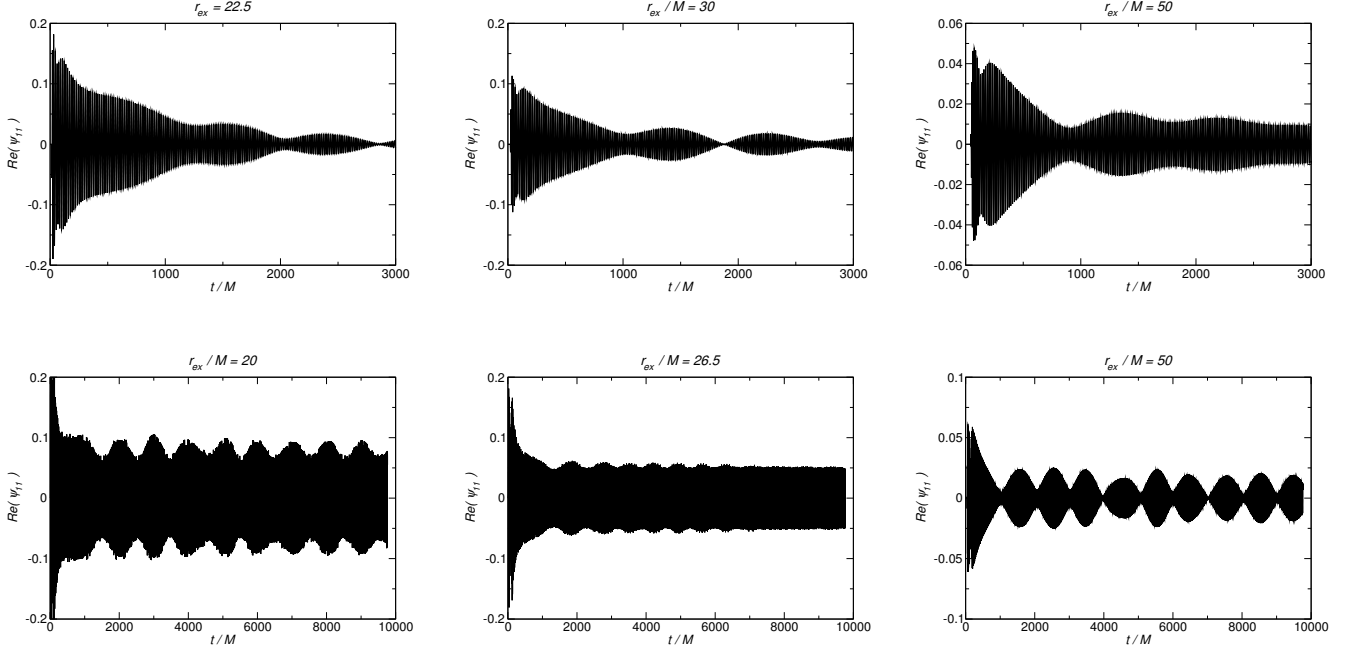


FIG. 6. Real part of the  $m = 1$  dipole obtained at selected extraction radii  $r_{\text{ex}}$  for a massive scalar field with  $M\mu_S = 0.42$  in a Schwarzschild (upper panels) and Kerr background with  $a = 0.99M$  (bottom panels). The location of the node of the first overtone is  $r_{\text{ex}} = 22.5 M$  for the Schwarzschild case (upper left most panel) and  $r_{\text{ex}} = 26.5 M$  for the Kerr case (bottom center panel).  $r_{\text{ex}} \sim 50 M$  corresponds to the overtone's local maximum in the Kerr case.

### 3. Massive scalar fields: mode excitation and beating

In addition to the well-known ringdown and decay, the evolution of massive Gaussian wave packets around BHs can exhibit more complex patterns. In particular, we expect massive scalar fields in Kerr backgrounds to eventually show exponential growth if they satisfy the superradiance condition Eq. (1) as well as  $\omega_R \leq \mu_S$ . The timescale for this instability, however, is of the order  $\gtrsim 10^7 M$  which is computationally too expensive to be realized within our numerical framework. In the following, we therefore focus on the complex signals observed at earlier times up to  $\sim 10^4 M$  in the evolution of massive scalar fields around Schwarzschild or Kerr black holes.

In particular, the time evolution of the  $l = m = 1$  mode of the scalar field with mass coupling  $M\mu_S = 0.42$  exhibits an oscillatory pattern with significant modulation of the amplitude. The quantitative behaviour of the oscillations, however, depends sensitively not only on the initial data but also on the radius where the modes are measured. This is illustrated in Fig. 6, where we show the  $m = 1$  dipole extracted at different radii for  $M\mu_S = 0.42$  considering a Schwarzschild or a Kerr BH background with  $a/M = 0.99$ . For each configuration shown in the figure, we have chosen three extraction radii, including the location  $r_{\text{node}}$  of the node,  $22.5 M$  and  $26.5 M$  respectively, for the Schwarzschild and Kerr case.

This phenomenon can be explained in terms of a beating modulation between two or more long-lived modes described by Eq. (38). This beating modulation depends on the relative strength of the different overtones which, in turn, depends on the extraction radius; for the case of a guitar string, for example, a specific mode cannot be excited at the location of its nodes. Our choice of initial parameters for this example did not involve any finetuning and we expect these features to be present in the time evolution of generic massive fields around BHs provided only that at least two long-lived modes are excited.

Our interpretation is confirmed by the Fourier spectra of the  $m = 1$  dipole obtained at different radii which are shown in Fig. 7 for the two background spacetimes. For the Kerr case with  $a/M = 0.99$  (right panel), we see that the signal is dominated by the fundamental mode at  $r_{\text{ex}} = 20 M < r_{\text{node}}$  and has two overtones of smaller amplitude. This is in agreement with the weakly modulated high frequency signal in the time evolution in the bottom left panel of Fig. 6. As expected, the amplitude modulation is particularly weak for  $r_{\text{ex}} = r_{\text{node}} = 26.5 M$  which coincides with the node of the first overtone. In fact, the small amount of modulation visible in the bottom center panel of Fig. 6

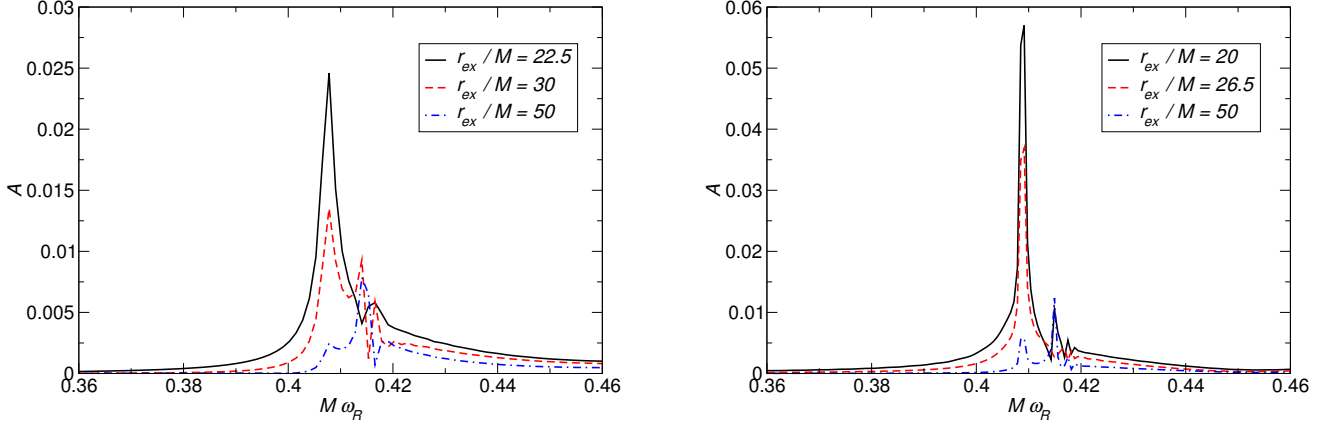


FIG. 7. Spectra of the  $l = m = 1$  mode of the massive scalar field with  $M\mu_S = 0.42$  evolved in the background of a Schwarzschild (left panel) or Kerr BH with  $a/M = 0.99$  (right panel). The lines correspond to the waveforms measured at different extraction radii. In particular,  $r_{ex} = 22.5 M$  (left) and  $r_{ex} = 26.5 M$  (right) correspond to the nodes of the first overtone.

at early times is mostly due to the *second* overtone which, however, damps out at later times. Then, the envelope is almost constant with a small growth rate  $M\omega_I \sim 10^{-7}$ , in order-of-magnitude agreement with previous studies [37, 44]. The situation is markedly different at  $r_{ex} = 50 M$ , where the first overtone has a local maximum and the comparable strength of fundamental mode and overtone result in the strong beating modulation displayed in the bottom right panel of Fig. 6. This analysis can be repeated for the non-rotating case, with similar conclusions. In contrast to the Kerr case, however, all modes decay resulting in overall damped signals.

Before proceeding with a detailed analysis of the beating modulation and mode excitation, we perform a convergence analysis of this setup which represents the most demanding and longest of our simulations. For this purpose, we have evolved the setup sK\_m042 using three different resolutions  $h_c = M/60$ ,  $h_m = M/72$  and  $h_h = M/84$ . We present the convergence plot, i.e. the differences between the coarse-medium and medium-high resolution runs in Fig. 8 for the monopole (left panel) and dipole (right panel). Our numerical results show second order convergence throughout the simulation. We estimate the discretization error to be about  $\Delta\psi_{11}/\psi_{11} \leq 1.1\%$  for the entire interval and  $\Delta\psi_{00}/\psi_{00} \leq 1\%$   $l = m = 0$  mode at early time which increases to  $\Delta\psi_{00}/\psi_{00} \leq 7\%$  at late times.

**Beating.** In order to better understand the beating pattern quantitatively, let us for simplicity consider the presence of only two modes with similar frequencies: the long-lived fundamental mode with frequency  $\omega_0 = \omega_{R,0} + i\omega_{I,0} \sim \omega_{R,0}$  and amplitude  $A_0$  and the first overtone with frequency  $\omega_1 = \omega_{R,0} + \delta_{10}$ , where  $\delta_{10} \ll 1$ , and amplitude  $A_1$ . The generalization to a larger number of modes is straightforward. For illustration, we explicitly list  $\delta_{10}$  for a selected subset of configurations in Table II. Because all these modes are long-lived, they are well approximated by pure sinusoids over short periods of time. The waveform  $\Psi$  is then described by the superposition

$$\Psi \sim (A_0 - A_1) \sin(\omega_{R,0}t) + A_1 \sin(\omega_{R,0}t) \cos(\delta_{10}t/2). \quad (42)$$

The modulation in amplitude is governed by the low-frequency signal  $\cos \delta_{10}t$  whereas the beating amplitude depends on the relative strength of the modes  $A_0, A_1$ . For equal amplitudes  $A_0 = A_1$ , for instance, the total signal is given by a sinusoid modulated by a cosine. The beating frequency  $\delta_{10}$  can be estimated by fitting the envelope of the total signal. For the two cases displayed in Fig. 6 we obtain  $\delta_{10} \sim 0.0074$  (for sS\_m042) and  $\delta_{n0} \sim 0.0063$  (for sK\_m042), in excellent agreement with the corresponding predictions listed in the third and fourth row of Table II.

This picture is confirmed by calculating the mode spectra from a Fourier transformation of the time series. The spectra thus obtained for the two configurations and different extraction radii are shown in Fig. 7 and each exhibit three pronounced peaks which correspond to the real parts of the fundamental and first two overtone QN frequencies. A spectral analysis applied to the Kerr case  $a/M = 0.99$  reveals  $\delta_{10} = 0.0063$  and  $\delta_{20} = 0.0087$ . Thus, the evolution of Gaussian initial data excites a third long-lived mode which is not listed in Table II. We have verified that this mode indeed exists, via a continued fraction scheme in the frequency domain, corresponding to  $M\omega = 0.41730 + i2.265 \times 10^{-8}$ .



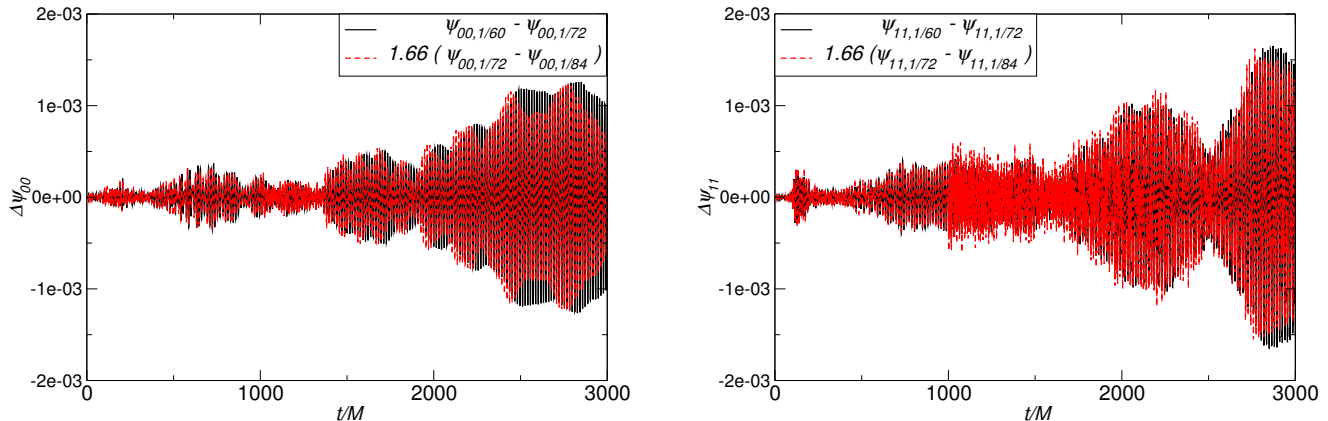


FIG. 8. Lower panels: Convergence plot of the  $l = m = 0$  (left panel) and  $l = m = 1$  (right panel) modes of simulation sK\_042. We present the differences between the coarse-medium and medium-high resolution runs, where the latter is amplified by  $Q_2 = 1.66$  indicating second order convergence.

**Mode excitation.** The mode excitation can be put on a more rigorous framework: Leaver’s seminal work, in particular, has established important results in this context and for further details we refer the reader to the original work [14] as well as comprehensive follow-up studies [9, 86, 87]. The upshot is that each quasi-normal mode, which corresponds to a pole in the complex-frequency plane, is excited to a different degree depending on the initial data and on the mode in question. The QNM contribution can be isolated from other features of the signal, such as the late-time tail, using the Green’s function technique [14, 86, 87]. In this formalism, the scalar field amplitude at intermediate times is given by a sum over quasinormal modes as

$$\Psi = \sum C_n e^{-i\omega_n t} \psi_n(\omega_n, r), \quad (43)$$

where  $\psi_n(\omega_n, r)$  is the quasinormal mode eigenfunction and  $\omega_n$  its frequency, both quantities can be computed via the Fourier-domain ordinary differential equation that governs massive scalars in the Kerr background [14, 86, 87]. The numbers  $C_n$ , called excitation coefficients characterize the amplitude to which each mode is excited. Two quantities are crucial to determine the excitation coefficients [87]: the behavior of  $\psi_n$  close to the eigenfrequency  $\omega_n$ , and the convolution of the eigenfunction  $\psi_n$  with the initial data. Thus, for instance, the relative amplitude between different modes depends strongly on the point where this amplitude is evaluated: if it is close to a node of one of the modes, the mode in question will have a very small amplitude: by definition a mode is not excited at its node. Likewise, localized initial data close to the node of the mode do not excite the mode in question, a well-known result for closed systems [87].

We have not attempted a complete quantitative understanding of mode excitation for this work, a preliminary analysis indicates that the excitation coefficients are indeed of comparable magnitude away from the nodes of the eigenmodes, but vary substantially close to the nodes.

#### IV. PROCA FIELD EVOLUTIONS

The evolution of vector fields, as for example the photon, are governed by Eq. (8b) which, after substitution of the definition  $F_{\mu\nu} = \nabla_\mu A_\nu - \nabla_\nu A_\mu$  and the Lorenz condition, Eq. (14), becomes rather similar to its scalar counterpart (8a). For this reason, it has been believed for a long time that massive vector fields should also be prone to a “BH bomb”-like superradiant instability. In fact, Rosa and Dolan [42] conjectured that instabilities of vector fields should not only be present but can be much stronger than those of scalar fields. This has recently been verified explicitly by Pani *et al* [40, 41] who derived the instability growth rates of massive vector fields in the slow-rotation approximation and found them to be several orders of magnitude larger than their scalar field counterparts. Their results, however, have been obtained only in the regime of slowly rotating black holes. Even though their results are conjectured to hold for arbitrary spins, a definitive answer to this question calls for the modelling of vector fields in generic Kerr

Run	$a/M$	$M\mu_V$	${}_{-1}\Sigma(\theta, \phi)$	$w/M$	Grid Setup
v1S_m000	0.00	0.00	Sup1	2.0	$\{(192, 96, 48, 24, 12, 6, 3, 1.5), h = M/60\}$
v2S_m000	0.00	0.00	Sup1	30.0	$\{(192, 96, 48, 24, 12, 6, 3, 1.5), h = M/60\}$
v1S_m010	0.00	0.10	Sup1	2.0	$\{(192, 96, 48, 24, 12, 6, 3, 1.5), h = M/60\}$
v1S_m020	0.00	0.20	Sup1	2.0	$\{(192, 96, 48, 24, 12, 6, 3, 1.5), h = M/60\}$
v2K1_m040	0.50	0.40	Sup2	30.0	$\{(1536, 384, 192, 96, 48, 24, 12, 6, 3, 1.5), h = M/60\}$
v1K2_m000	0.99	0.00	Sup1	2.0	$\{(192, 96, 48, 24, 12, 6, 3, 1.5), h = M/96\}$
v2K2_m040	0.99	0.40	Sup1	30.0	$\{(1536, 384, 192, 96, 48, 24, 12, 6, 3, 1.5), h = M/64\}$
v2K2_m042	0.99	0.42	Sup1	30.0	$\{(1536, 384, 192, 96, 48, 24, 12, 6, 3, 1.5), h = M/64\}$
v2K2_m044	0.99	0.44	Sup1	30.0	$\{(1536, 384, 192, 96, 48, 24, 12, 6, 3, 1.5), h = M/64\}$
v1K2_m100	0.99	1.00	Sup1	2.0	$\{(1536, 384, 192, 96, 48, 24, 12, 6, 3, 1.5), h = M/60\}$

TABLE III. Initial setup for simulations of Proca fields with mass coupling  $M\mu_V$  in BH background with dimensionless spin parameter  $a/M$ . The initial Gaussian pulse with width  $w/M$  is located at  $r_0 = 12 M$  and consists of a superposition of  $s = -1$  spin-weighted spherical harmonics given by Eq. (44a) (“Sup1”) or Eq. (44b) (“Sup2”). We further denote the grid setup, in units of the BH mass  $M$  following the notation of Sec. II E in [72].

geometries. In the frequency domain, such modelling represents a formidable challenge because the equations of motion appear to be non-separable. Here we therefore address this question in the framework of numerical evolutions in the time domain, where the non-separability of the equations does not represent a serious obstacle.

For this purpose, we prescribe initial data in the form of a superposition of Gaussian pulses centered around  $r_0 = 12 M$  and composed of several multipoles with angular dependence given by  $s = -1$  spin-weighted spherical harmonics  ${}_{-1}Y_{lm}$ . Specifically, we have chosen linear combinations

$$\begin{aligned}
{}_{-1}\Sigma(\theta, \phi) = & -\frac{1}{\sqrt{3}}({}_{-1}Y_{1-1} + {}_{-1}Y_{11}) - \frac{1}{\sqrt{5}}({}_{-1}Y_{2-1} - {}_{-1}Y_{21}) - \frac{1}{\sqrt{6}}{}_{-1}Y_{10} - \frac{1}{\sqrt{30}}{}_{-1}Y_{20} \\
& - \frac{1}{3\sqrt{5}}({}_{-1}Y_{2-2} - {}_{-1}Y_{22}) - \frac{\sqrt{2}}{3\sqrt{35}}({}_{-1}Y_{3-2} + {}_{-1}Y_{32}), \tag{44a}
\end{aligned}$$

$${}_{-1}\Sigma(\theta, \phi) = -\frac{1}{\sqrt{3}}({}_{-1}Y_{1-1} + {}_{-1}Y_{11}) - \frac{1}{\sqrt{5}}({}_{-1}Y_{2-1} - {}_{-1}Y_{21}), \tag{44b}$$

such that the imaginary parts of the fields vanish. By virtue of the evolution equations (20a)-(20c), purely real initial data remain real throughout the evolution so that our choice reduces the computational requirements to evolving only seven – instead of 14 – independent variables. We have summarized the initial configurations of our set of simulations together with the grid setup in Table III. In order to analyse the time evolutions of the vector field  $A_\mu$ , we decompose its time component  $\varphi$  and the Newman-Penrose scalar  $\Phi_2$ , constructed from the spatial components according to Eq. (32), into multipoles by projecting them onto spherical harmonics with spin weight  $s = 0$  and  $s = -1$ , respectively.

### A. Massless vector fields

We first study the behaviour of massless vector field perturbations with  $M\mu_V = 0$ . This case has been studied extensively in the literature [9] and therefore also enables us to compare our findings with previous investigations. Our results for massless Proca fields are summarized in Table IV and Figs. 9 and 10. Let us first consider the simplest case of a massless vector field in Schwarzschild background. The time evolutions of the  $l = m = 1$  multipole obtained for initial Gaussian pulses of width  $w = 2 M$  and  $w = 30 M$  are shown in Fig. 9. For the narrow pulse (solid curve in the figure) we clearly identify the pattern familiar from our scalar field evolutions in Sec. III B: an early transient whose details depend on the initial configuration is followed by a quasi-normal ringing characterized entirely by the BH parameters and a late-time tail. For an initially broad pulse (red dashed curve), however, the initial transient is directly followed by a power-law tail with no visible intermediate ringdown stage. This feature has been reported for scalar fields in Refs. [86, 89] and is a consequence of the negligible excitation of the long-lived fundamental mode and low overtones by broad pulses; the high overtones which are excited significantly by this type of initial data rapidly decay before the transient gives way for a clear QN ringdown pattern to emerge.

For a quantitative comparison with calculations performed in the frequency domain, we have fitted the ringdown part of our numerically extracted multipoles for the case of a narrow initial Gaussian with exponentially damped

$a/M$ ( $lm$ )	$M\omega_{lm}^{\text{fd}}$	$M\omega_{lm}^{\text{num}}$
0.00 (10)	$0.2483 - i0.0925$	$0.248 - i0.092$
0.00 (20)	$0.4576 - i0.0950$	$0.455 - i0.093$
0.99 (10)	$0.2743 - i0.0759$	$0.274 - i0.075$
0.99 (11)	$0.4634 - i0.0313$	$0.464 - i0.033$
0.99 (20)	$0.4999 - i0.0800$	$0.498 - i0.079$
0.99 (22)	$0.9099 - i0.0301$	$0.887 - i0.037$

TABLE IV. Quasi-normal mode frequencies of massless vector perturbations in a Schwarzschild or Kerr BH background with  $a/M = 0.99$ . The values for  $M\omega_{lm}^{\text{num}}$  have been obtained from fits to our numerical evolution of the field, whereas those for  $M\omega_{lm}^{\text{fd}}$  have been computed with the continued fraction method [9, 11, 88].

sinusoids. The resulting complex frequencies  $\omega_{lm}^{\text{num}}$  are listed in Table IV and agree well with the values  $\omega_{lm}^{\text{fd}}$  obtained from frequency-domain calculations [9, 11, 14, 88].

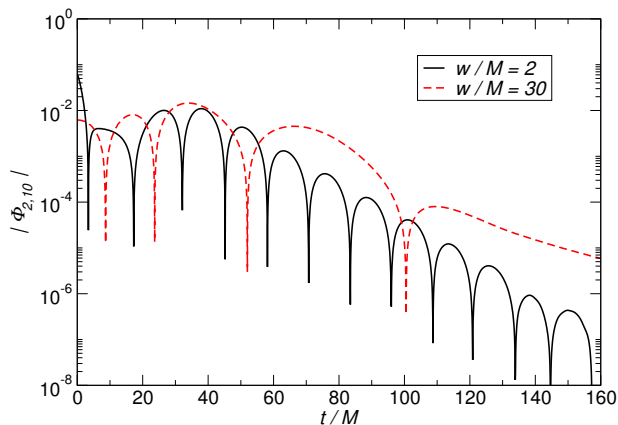


FIG. 9. The  $l = 1, m = 0$  multipole of  $\Phi_2$ , extracted at  $r_{\text{ex}} = 10 M$  from the time evolution of a Gaussian pulse of width  $w = 2 M$  (black solid line) and  $w = 30 M$  (red dashed line) around a Schwarzschild BH.

The time evolution of a massless vector field initialized as a narrow Gaussian of width  $w = 2 M$  around a rapidly spinning Kerr BH with  $a/M = 0.99$  is displayed in Fig. 10 and qualitatively agrees with the corresponding simulation around a Schwarzschild background. Note, however that the quasi-normal ringdown is significantly slower for the spinning case which is also reflected by the relatively small imaginary quasi-normal mode frequencies listed for this case in Table IV. Accurately measuring such small imaginary components in numerical simulations represents a considerable challenge which is why we have chosen a higher numerical resolution for this particular simulation; cf. Table III. We thus obtain agreement of a few % with frequency-domain predictions for the imaginary part. In contrast the real part of the frequency is much easier to extract numerically and shows excellent agreement around 1 % or less with the values calculated in the frequency domain.

### B. Proca field in Schwarzschild backgrounds and in the slow-rotating limit

We now consider time evolutions of massive vector, or Proca, fields in a Schwarzschild background. For this purpose, we choose the mass parameters  $M\mu_V = 0.1$  and  $M\mu_V = 0.2$  which allow for a direct comparison with recent QNM computations by Rosa & Dolan [42] and Pani *et al* [40, 41]. In contrast to the massive scalar field, the Proca field has three degrees of freedom and the resulting radiation multipoles can be classified into three groups: axial modes with spin  $s = 0$  and two polar modes with  $s = \pm 1$ . Following Refs. [40–42], we denote  $s = 0$  multipoles as *even scalars* (ES) and the  $s = +1, -1$  as *odd* (O) and *even vector* (EV), respectively. We emphasize that these three different degrees

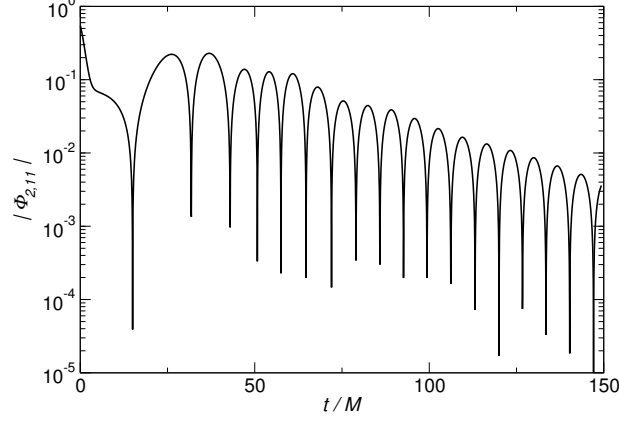


FIG. 10. Time evolution of the  $l = m = 1$  mode of  $\Phi_2$  of run v1K2\_m000, i.e., a massless vector field in a Kerr background with  $a/M = 0.99$  extracted at  $r_{\text{ex}} = 10 M$ .

$l$	$M\omega_{l0}^{\text{fd}}$ (ES)	$M\omega_{l0}^{\text{fd}}$ (O)	$M\omega_{l0}^{\text{fd}}$ (EV)	$M\omega_{l0}^{\text{num}}$ ( $\varphi_l$ )	$M\omega_{l0}^{\text{num}}$ ( $\Phi_{2,l}$ )	$p$ ( $\varphi_{l0}$ )	$p$ ( $\Phi_{2,l0}$ )
0	$0.1216 - i0.0791$			$0.125 - i0.080$		1.51	
1	$0.3054 - i0.0914$	$0.2435 - i0.0944$	$0.2539 - i0.0887$	$0.245 - i0.098$	$0.252 - i0.087$	0.49	0.49
2	$0.4921 - i0.0943$	$0.4552 - i0.0955$	$0.4610 - i0.0938$	$0.462 - i0.091$	$0.452 - i0.096$	0.48	0.49

TABLE V. QNM frequencies and tail exponents for Proca field perturbations in the Schwarzschild background, for  $M\mu_V = 0.1$ . Modes  $\omega^{\text{fd}}$  have been computed with the continued fraction and forward-integration method in the frequency domain [40–42]. These modes are divided in odd (O), even scalar (ES) and even vector (EV) parity; see text for details. The QNM frequencies extracted from our numerical simulations are shown as  $\omega^{\text{num}}$ , as extracted from  $\varphi_{l0}$  and  $\Phi_{2,l0}$ . Finally, we also show the decay exponent  $p$  of the oscillatory tail; c. f. Eq. (45).

of freedom have different spectra except for the massless case where the spectra of the vector modes are degenerate while the scalar mode reduces to a gauge field [9, 42, 88]. The quasi-normal ringdown frequencies  $\omega_{lm}^{\text{fd}}$  obtained from frequency-domain calculations for the three types of multipoles are shown in Table V for  $M\mu_V = 0.1$  considering a Schwarzschild background.

In order to obtain numerical estimates for the frequencies, we have evolved Gaussian initial data of width  $w = 2 M$  centered around  $r_0 = 12 M$  for our two choices of  $M\mu_V = 0.1$  and  $0.2$ . The resulting dipoles of  $\Phi_2$  extracted at  $r_{\text{ex}} = 10 M$  are shown in Fig. 11 and reveal the by now familiar pattern of early transient, ringdown and tail. Fitting an exponentially damped sinusoid to the ringdown part of the dipoles of  $\Phi_2$  (solid curve in the figure) as well as the scalar component  $\varphi$  for the case  $M\mu = 0.1$  yields numerical estimates for the frequencies listed in Table V as  $\omega_{lm}^{\text{num}}$ . These estimates agree with the frequency-domain predictions within a few percent or less. Note, however, that the frequencies for some types of modes are very similar, so that we cannot unambiguously identify which modes are excited by our particular choice of initial data. For  $l = 2$ , for instance, our numerical results are compatible with both, an odd or even vector mode.

In Fig. 11 we see that from time  $t \sim 100 M$  onwards, the signal is dominated by the tails whose functional form is given by a decaying sinusoid of the form [90]

$$\Phi \sim t^{-(l+p)} \sin(\mu_V t), \quad (45)$$

at intermediate times, where  $p = 3/2 + s$  depends on the spin, or parity, of the mode. At late times, on the other hand, the signal is expected to follow the universal behaviour

$$\Phi \sim t^{-5/6} \sin(\mu_V t), \quad (46)$$

independent of the spin  $s$  of the field [81, 82, 90]. Numerical estimates for the exponent  $p$  extracted from our numerical results for  $\Phi_2$  and  $\varphi$  are shown in Table V and are in excellent agreement with the prediction  $p = 3/2 + s$  for intermediate

times and spin values  $s = 0$  for the monopole and  $s = -1$  for dipole and quadrupole. A similar analysis for the larger mass parameter  $M\mu = 0.2$  also leads to good agreement between numerical and frequency-domain results, albeit with slightly larger discrepancies of  $\lesssim 7\%$ .

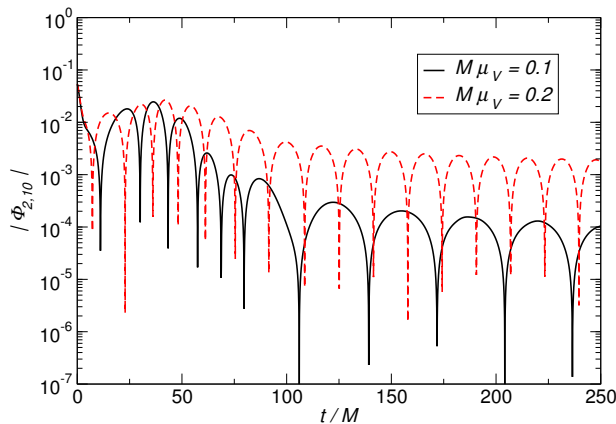


FIG. 11. Time evolution of the Proca field with mass coupling  $M\mu_V = 0.1$  (black solid line) and  $M\mu_V = 0.2$  (red dashed line) in a Schwarzschild background. We show the  $l = 1, m = 0$  multipole of the Newman-Penrose scalar  $\Phi_2$ , extracted at  $r_{\text{ex}} = 10 M$ .

Before we discuss in detail the behaviour of Proca fields in rapidly rotating Kerr backgrounds, we briefly test our code in the case of a smaller rotation rate  $a/M = 0.5$  where the slow-rotation approximation of [40, 41] is expected to provide rather accurate results. For this purpose, we have evolved a Proca field with a mass parameter  $M\mu_V = 0.4$  (simulation v2K1.m040 in Table III) which can be shown to result in a *stable* mode, i.e., it does not satisfy the superradiance criterion (1). For this configuration we observe an extended transient resulting from the wave packet impinging on the black hole followed by a slowly decaying QN ringdown signal after  $t \sim 200 M$ . Fitting a damped sinusoid to this ringdown part, we find a ringdown frequency  $M\omega_{11} = 0.389 - i0.0023$  in excellent agreement with semi-analytic calculations in the slow-rotation approximation [40, 41].

### C. Instability of Proca fields in highly spinning Kerr backgrounds

According to the superradiant condition (1), rapidly rotating black holes are most likely to induce superradiance phenomena in ambient vector fields and we therefore discuss the case of Proca fields in a Kerr background with  $a/M = 0.99$  in this section. In fact, recent calculations [40, 41] indicate that the maximum instability growth rate is realized in this background spacetime for a mass parameter of about  $M\mu_V = 0.4$  and our discussion will focus on this case supplemented by additional simulations with  $M\mu_V = 0.42, 0.44$  and  $1.0$ . The time evolution of the  $l = m = 1$  multipole of the Newman-Penrose scalar  $\Phi_2$  as well as the scalar component  $\varphi$  obtained for the case  $M\mu_V = 0.4$  is shown for several choices of the extraction radius  $r_{\text{ex}}$  in Fig. 12. Animations of the numerical evolutions are available online [85].

**Beating of modes.** The time evolutions of the Proca field shown in Fig. 12 reveal strong amplitude modulations similar to those observed for scalar fields in Fig. 6. They also depend sensitively on the location of the measurement specified by the extraction radius  $r_{\text{ex}}$  and, again, we interpret this feature as a beating effect. In order to study this in more detail, we have computed the Fourier spectra of the waveforms at different radii and show the results in Fig. 13. The curves clearly reveal several peaks corresponding to separate mode contributions (fundamental mode or overtones) of the dipole field and the relative amplitude of these peaks varies significantly with extraction radius. Consider, for example, the spectrum of the dipole of  $\Phi_2$  in the left panel of Fig. 13: At  $r_{\text{ex}} = 10 M$  the amplitude of the lowest frequency mode is about two thirds of the amplitude of the strongest peak near  $M\omega_R = 0.39$ , but its relative strength rapidly decreases at larger extraction radii. This is also reflected in the observed time evolutions of the  $\Phi_2$  dipole in the upper panels of Fig. 12: the waveform extracted at  $r_{\text{ex}} = 10 M$  exhibits a high frequency modulation which is weakly present at  $r_{\text{ex}} = 25 M$  and entirely absent in the waveform measured at  $r_{\text{ex}} = 40 M$ .

Likewise, the high-frequency modulation of the time component  $\varphi$  weakens at larger radii as the relative amplitude of the two lowest peaks in the spectrum (right panel of Fig. 13) decreases.

There remains one important issue: which conditions lead to the beating of modes? While beating is expected to be a generic feature, it is not always excited. Here, we attempt to determine indicators for the (non-)observability of beating effects. Because we have performed a multipole expansion of the fields, and beating is present on a fixed multipole, then clearly a beating pattern requires the excitation of different overtones. For this reason, a modulation of the amplitude is only triggered by evolutions of generic initial pulses<sup>3</sup>. Furthermore, our numerical simulations indicate no dependence on the background spacetime; Fig. 6 shows beating effects of the scalar field around Schwarzschild and Kerr BHs. Beating is therefore *not* related to superradiance. On the other hand, the excitation of different modes is merely a necessary condition but not sufficient to trigger amplitude modulations. This becomes evident in the evolutions of Gaussian initial data for the vector field with small mass parameters in a Schwarzschild background which only exhibit a quasi-normal ringdown and tail. In order to shed further light on this question, we therefore consider the entire set of Proca evolutions in BH backgrounds and summarize our results as follows: (i) We do not observe beating nor any long-lived modes for mass parameters  $M\mu_V = 0.1, 0.2$  in Schwarzschild background; (ii) we observe beating in the dipole mode for  $M\mu_V = 0.4, 0.42, 0.44$  in rapidly rotating Kerr; (iii) we observe beating in the quadrupole but not in the dipole for  $M\mu_V = 1.0$  in the background of a highly spinning Kerr BH. Let us first consider in our interpretation of these observations the case of small mass parameters  $M\mu_{S,V}$ . The absence of long-lived modes in our simulations is most likely a consequence of low-mass bound states being concentrated far from the black holes. For our choice of initial Gaussian pulses centered around  $r_0 = 12 M$ , these states are therefore only weakly excited and play no significant role in the evolution. Furthermore, beating patterns for small mass parameters have particularly large periods. We can therefore not rule out that amplitude modulations might become visible in these evolutions at late times far larger than the evolution times feasible with our numerical framework. We suspect a similar reason is behind our not observing beating modulation in the dipole mode in case of large mass coupling  $M\mu_V = 1$ . We therefore tentatively conclude that two conditions need to be met in addition to the presence of at least two modes in order to observe beating on time scales of  $\sim 10^4 M$ . (i) the bound states must not be localized far away from the peak of the initial data and (ii) beating periods need to be sufficiently short.

**Instability of Proca fields around Kerr.** The most striking feature of the time evolutions in Fig. 12 is the amplitude growth of the signal over time (ignoring the early transient stage). We interpret this growth as a signature of the superradiant instability of massive vector fields and estimate the growth rate of the  $m = 1$  dipole of  $\Phi_2$  obtained for  $M\mu_V = 0.4$  and  $a/M = 0.99$  as

$$M\omega_I \sim (5 \pm 1) \cdot 10^{-4} \quad \rightarrow \quad \frac{\tau}{M} \sim (3.3 \pm 1.7) \times 10^3, \quad (47)$$

and about half that value for the instability rate of  $\varphi$ . We believe the discrepancy of the growth rates of  $\Phi_2$  and  $\varphi$  is due to the different growth scales of the axial and polar sector and the fact that  $\varphi$  only sees the axial sector. We note that our estimates for the growth rates are of the same order of magnitude as the value  $\tau/M \sim 10^3$  derived from extrapolation of slow-rotation calculations; cf. Eq. (98) in Ref. [41] and Fig. 2 in Ref. [40]. The superradiant instability time scales for vector fields are thus up to four orders of magnitude larger than those of their scalar counter parts which renders possible their identification in the numerical evolutions presented in this work.

## V. CONCLUSIONS

We have performed an extended study of the time evolution of massless and massive scalar and vector fields in Schwarzschild and Kerr BH background spacetimes with spin parameters up to  $a/M = 0.99$ . Our results are consistent with published results obtained in the frequency domain in so far as these are available. For evolutions involving exclusively short-lived modes, we observe the known pattern of an initial transient followed by an exponentially damped ringdown phase and late-time tails.

For the case of massive fields, there exists a second class of long-lived modes called bound states whose evolution exhibits a significantly richer structure. In particular, we have identified a beating pattern caused by the interference of different modes (the fundamental mode and overtones) as manifest in the Fourier spectra calculated from the time evolutions. The relative amplitude of different modes in the spectra and, thus, the specific shape of the beating pattern strongly depends on the observation radius. We believe that these beating effects provide an explanation for an apparent discrepancy between time and frequency domain calculations of instability growth rates of scalar

---

<sup>3</sup> as opposed to pure bound states. It is important to note that by pure bound states we mean stationary solutions of the linearized field equations in the Kerr background; therefore effects such as mode coupling are already taken into account: pure modes do not couple to other multipoles when the expansion basis is taken to be spheroidal harmonics.

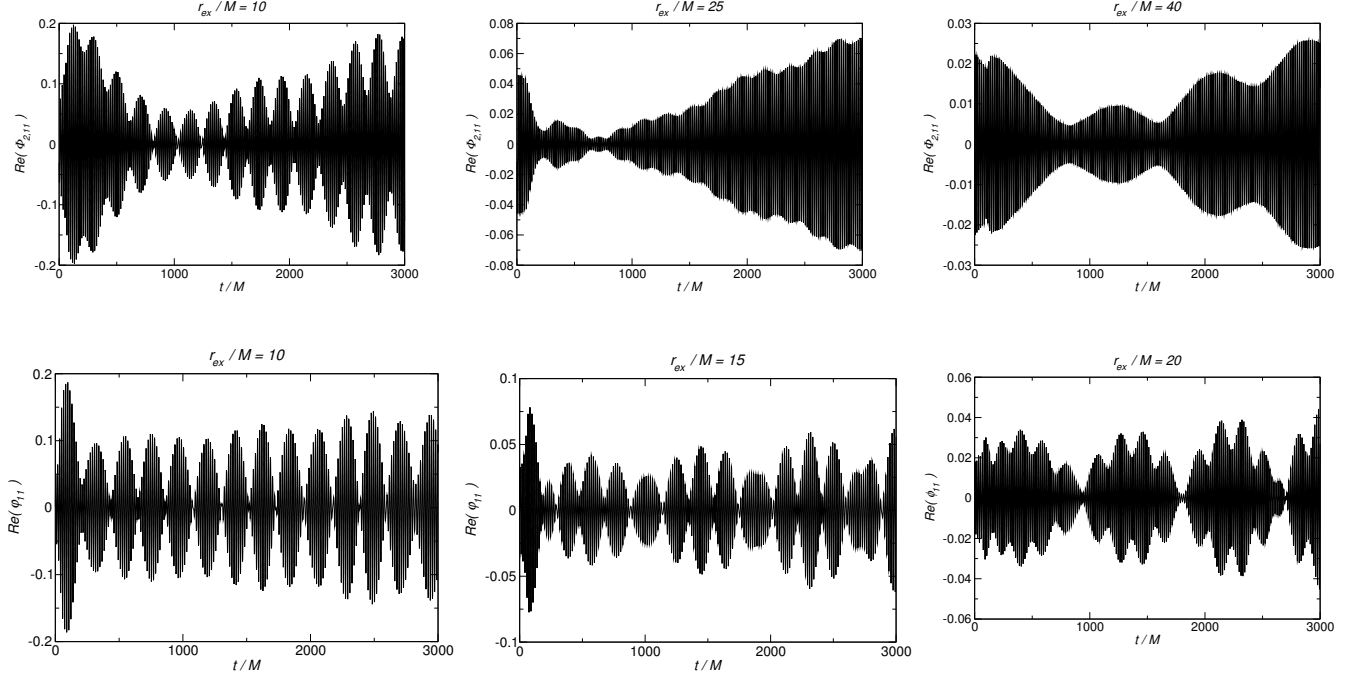


FIG. 12. Time evolution of the Proca field with mass coupling  $M\mu_V = 0.40$  in Kerr background with  $a/M = 0.99$ , at different extraction radii. We plot the  $l = m = 1$  mode of the Newman-Penrose scalar  $\Phi_2$  (upper panels) and of the scalar component  $\varphi$  (lower panels).

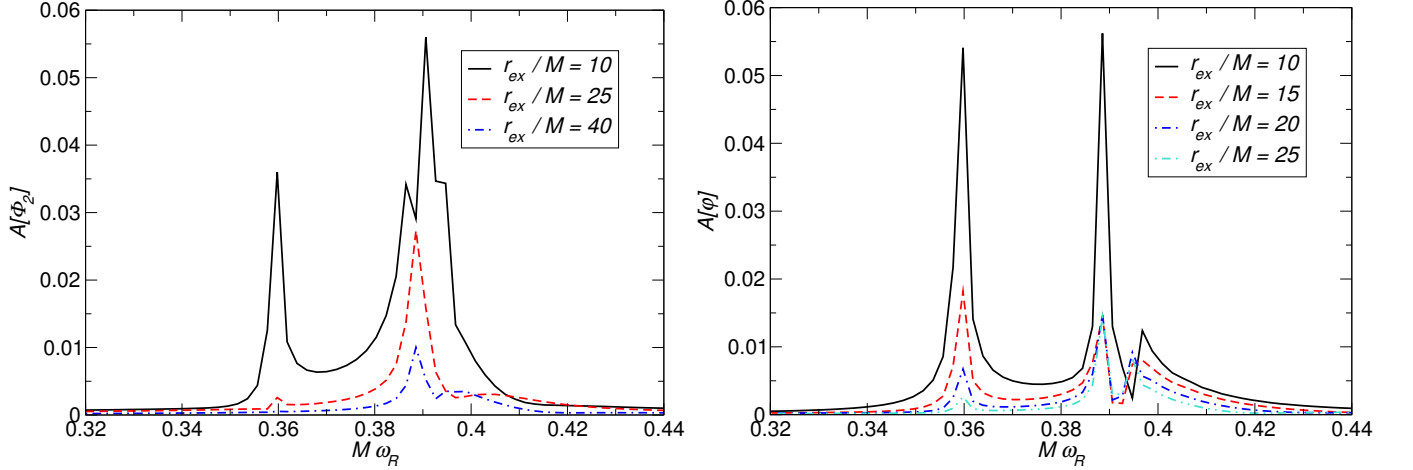


FIG. 13. Spectra of the  $l = m = 1$  mode of the Newman-Penrose scalar  $\Phi_2$  (left panel) and of the scalar component  $\varphi$  (right panel) excited by the Proca field with mass coupling  $M\mu_V = 0.40$  in Kerr background with  $a/M = 0.99$ . Different lines correspond to the waveforms measured at different extraction radii.

fields around Kerr backgrounds. Specifically, Ref. [60] (see their Fig. 3) reported a time evolution lasting about  $3 \times 10^3 M$  of a massive scalar field with  $M\mu_S = 0.25$  in a Kerr background with  $a/M = 0.9999$  and obtained a growth timescale approximately two orders of magnitude smaller than that predicted by frequency-domain calculations. For this particular configuration, the frequency-domain estimate, Eq. (38), predicts a beating period  $\tau \sim 5 \times 10^3 M$ , about the entire duration of their time evolution, and we believe that their estimate of the growth rate was correspondingly contaminated by the resulting amplitude modulation.

Based on our numerical results, we conjecture that two conditions are required for the presence of beating: (i)

generic initial configurations of massive fields as opposed to single-frequency bound state initial data, and (ii) initial data able to excite these bound states. For extremely small masses for instance, the bound states are localized far from the BH. Accordingly, initial data peaked far from the BH would be required to excite them.

In an accompanying paper Dolan [61] has investigated the massive scalar field instability as well as a system involving massless scalars but enclosed by a mirror in the time domain. Specifically, the author employs a “coupled  $1+1$  dimensional” numerical scheme which allows for significantly longer evolution times up to  $t \sim 10^6 M$ . This work finds bound state frequencies and instability time scales in excellent agreement with frequency domain calculations and, due to the generic initial configurations, confirms/ supports our findings of the beating phenomena.

Finally, we have confirmed the existence of superradiant unstable massive vector fields around rapidly spinning BHs. In contrast to massive scalar fields, the instability of Proca fields is stronger by about four orders of magnitude leading to growth times as short as  $\tau/M \sim 3.3 \times 10^3$  in rapidly spinning Kerr BH backgrounds. It is instructive to translate this number for the case of realistic astrophysical black hole candidates. For a solar mass BH and a supermassive BH of the size of SagittariusA\* ( $M \sim 4.1 \cdot 10^6 M_\odot$ ) at the center of our galaxy we obtain timescales of  $\tau \sim 9$  ms and  $\tau \sim 4 \cdot 10^4$  s, respectively.

It has been argued by Pani *et al.* [40] that the angular momentum thus extracted from the black hole provides a mechanism to observationally constrain the mass of the photon. In view of the short time scales even for a supermassive black holes, spin measurements of the BH at the center of the Milky Way, may indeed constrain the photon mass to unprecedented levels. The exciting prospect of using large, supermassive black holes to understand the microscopic world raises several questions:

- (1) Influence of accretion disks. Astrophysical black holes are not isolated, but typically are surrounded by accretion disks. Can the interaction with matter kill the instability? It was argued previously [40] that the superradiant instability is a global mode, on scales larger than the BH. On these scales matter is electrically neutral, and the coupling should be negligible. Therefore, it is not likely that (thin) accretion disks can quench the instability; thin disks are expected to lie along the equator of a Kerr BH and are not expected to interact strongly with boson clouds that extend well off the equator. The influence of thick disks or other effects is unknown at the moment, but it is surely important to study these effects in more detail.
- (2) Self-interacting scalar fields: One class of interesting problems involves massive scalar fields whose dynamics are described by additional non-linear terms, modelling their self-interaction. This open issue has first been addressed by Yoshino & Kodama [44] who modelled the collapse of a so-called bosonova.
- (3) Backreaction effects: As far as we are aware, all studies exploring massive fields have been performed in the linear regime. Therefore it is of utmost interest to explore the fully non-linear regime, which allows for the investigation of the backreaction of the spacetime, such as the spin-down of the BH due to (subsequent) superradiant scattering. This type of studies would enable us to glance at the end-state of the superradiant instability or, possibly, equilibrium configurations.

The present study marks crucial first steps to explore an entire playground of exciting future applications of massive fields in BH spacetimes.

Animations of the evolutions can be found online [85].

## VI. ACKNOWLEDGEMENTS

We thank Sam Dolan, Paolo Pani and João Rosa for useful comments and discussions and for making their data available to us. We are indebted to Hideo Kodama and Hirotaka Yoshino for explanations regarding time-evolution of bound states. We thank Gaurav Khanna for useful correspondence. We are especially indebted to Sérgio Almeida for all his hard work on the “Baltasar Sete-Sóis” cluster. We thank all participants of the YITP-T-11-08 workshop on “Recent advances in numerical and analytical methods for black hole dynamics” for useful discussions. We thank the Yukawa Institute for Theoretical Physics at Kyoto University for their kind hospitality during the early stages of this work. This work was supported by the *DyBHo-256667* ERC Starting Grant, the NRHEP-295189 FP7-PEOPLE-2011-IRSES Grant, the *CBHEO-293412* FP7-PEOPLE-2011-CIG Grant, the *ERC-2011-StG 279363-HiDGR* ERC Starting Grant, and by FCT - Portugal through PTDC projects FIS/098025/2008, FIS/098032/2008, CTE-ST/098034/2008, CERN/FP/123593/2011. H.W. is funded by FCT through grant SFRH/BD/46061/2008. U.S. acknowledges support by the from the Ramón y Cajal Programme and Grant FIS2011-30145-C03-03 of the Ministry of Education and Science of Spain. A.I. was supported by JSPS Grant-in-Aid for Scientific Research Fund (C) 22540299 and (A) 22244030.

Computations were performed on the “Baltasar Sete-Sois” cluster at IST, the cane cluster in Poland through PRACE DECI-7 “Black hole dynamics in metric theories of gravity”, on MareNostrum in Barcelona through BSC grant AECT-2012-2-0005, on Altamira in Cantabria through BSC grant AECT-2012-3-0012, on Caesaraugusta in Zaragoza through BSC grants AECT-2012-2-0014 and AECT-2012-3-0011, XSEDE clusters SDSC Trestles and NICS Kraken through



NSF Grant No. PHY-090003, Finis Terrae through Grant CESGA-ICTS-234 and the COSMOS supercomputer, part of the DiRAC HPC Facility which is funded by STFC and BIS. The authors thankfully acknowledge the computer resources, technical expertise and assistance provided by the Barcelona Supercomputing Centre—Centro Nacional de Supercomputación and by Andrey Kaliazlin for computational support and technical advice with COSMOS.

### Appendix A: Flux formula

From the Lagrangian  $\mathcal{L}$ ,

$$\frac{1}{\sqrt{-g}}\mathcal{L} := -\frac{1}{2}g^{\mu\nu}\Psi^*_{,\mu}\Psi_{,\nu} - \frac{\mu_S^2}{2}\Psi^*\Psi - V(\Psi) - \frac{1}{4}F^{\mu\nu}F_{\mu\nu} - \frac{\mu_V^2}{2}A_\nu A^\nu - \frac{k_{\text{axion}}}{2}\Psi^*F^{\mu\nu}F_{\mu\nu} + J_\nu^{(S)}A^\nu, \quad (\text{A1})$$

we obtain, under the Lorenz condition (14), the equations of motion

$$(\nabla^\mu\nabla_\mu - \mu_S^2)\Psi - \frac{k_{\text{axion}}}{2}F^{\mu\nu}F_{\mu\nu} - V'(\Psi) = 0 \quad (\text{A2})$$

$$(\nabla^\mu\nabla_\mu - \mu_V^2)A^\nu - R_\mu{}^\nu A^\mu - 2k_{\text{axion}}F^{\nu\mu}\nabla_\mu\Psi = -J^{(S)\nu} \quad (\text{A3})$$

and the stress-energy tensor

$$T_{\mu\nu} = T_{\mu\nu}^A + T_{\mu\nu}^\Psi, \quad (\text{A4})$$

$$T_{\mu\nu}^A := F_{\mu\alpha}F_\nu{}^\alpha - \frac{1}{4}g_{\mu\nu}F_{\alpha\beta}F^{\alpha\beta} + \mu_V^2 A_\mu A_\nu - \frac{1}{2}\mu_V^2 A^\alpha A_\alpha g_{\mu\nu}, \quad (\text{A5})$$

$$T_{\mu\nu}^\Psi := \frac{1}{2}(\nabla_\mu\Psi^*\nabla_\nu\Psi + \nabla_\mu\Psi\nabla_\nu\Psi^*) - \frac{1}{2}g_{\mu\nu}(\nabla_\mu\Psi^*\nabla^\mu\Psi + \mu_S^2\Psi^*\Psi + 2V(\Psi)). \quad (\text{A6})$$

Note that the Chern-Simons term does not alter the stress-energy tensor.

We are concerned with stationary axisymmetric spacetimes. Let us denote by  $t^\mu$  and  $\phi^\mu$ , respectively, the stationary and the axisymmetric Killing field. The rigidity theorem states that there exists a Killing vector field  $\chi^\mu$ , which is normal to, hence null on, the horizon  $\mathcal{H}^+$ . Such a Killing vector field is given by the combination of  $t^\mu$  and  $\phi^\mu$ ,

$$\chi^\mu = t^\mu + \Omega_H \phi^\mu, \quad (\text{A7})$$

where  $\Omega_H$  denotes the angular velocity of the Killing horizon of the black hole, and for the Kerr metric

$$\Omega_H = \frac{a}{r_+^2 + a^2}, \quad (\text{A8})$$

with  $r_+$  being the horizon radius  $r_+ = M + \sqrt{M^2 - a^2}$  in the Boyer-Lindquist coordinates.

Let us introduce the energy current  $J_\mu$  by

$$J_\mu = -T_{\mu\nu}t^\nu = -T_{\mu\nu}^\Psi t^\nu - T_{\mu\nu}^A t^\nu, \quad (\text{A9})$$

and consider two time-slices  $\Sigma_1$  and  $\Sigma_2 \subset \{J^+(\Sigma_1) \setminus \Sigma_1\}$ , which intersect the event horizon  $\mathcal{H}^+$  at  $t = t_1$  and  $t = t_2$ , respectively. (One may view  $t$  as the Killing parameter of  $t^\mu$ ). Then the energy flux  $\mathcal{F}$  that flows into the black hole in the time-interval  $\mathcal{I} = \{\mathcal{H}^+ : t_1 < t < t_2\}$  is given by

$$\begin{aligned} \mathcal{F} &= \int_{\Sigma_2} d\Sigma^\mu J_\mu - \int_{\Sigma_1} d\Sigma^\mu J_\mu = \int_{\mathcal{I}} dN n^\mu J_\mu \\ &= - \int_{\mathcal{I}} dN \chi^\mu J_\mu = \int_H dS \langle \chi^\mu t^\nu T_{\mu\nu} \rangle. \end{aligned} \quad (\text{A10})$$

Here  $n^\mu$  denotes the normal to  $\mathcal{H}^+$ ,  $dN$  the volume element of the horizon  $\mathcal{H}^+$ , and  $dS$  the area element of the cross-section  $H = \mathcal{H}^+ \cap \Sigma$ , and  $\langle \cdot \rangle$  expresses the time average along the horizon. Superradiant scattering occurs when the energy flux going into the horizon becomes negative:

$$\mathcal{F} < 0. \quad (\text{A11})$$

We consider below the flux with respect to the scalar field and the vector field separately. For the scalar field, the mode decomposition is defined by

$$\mathcal{L}_t \Psi = -i\omega \Psi, \quad \mathcal{L}_\phi \Psi = im \Psi, \quad (\text{A12})$$

where  $\omega$  denotes the frequency and  $m$  the angular quantum number. It implies, in particular,

$$\mathcal{L}_\chi \Psi = -i(\omega - m\Omega_H) \Psi. \quad (\text{A13})$$

Then, substituting (A6) into (A10) and using the fact that  $g_{\mu\nu} t^\nu \chi^\mu = 0$  on the horizon, we can immediately find the flux formula for  $\Psi$ :

$$\mathcal{F}^\Psi = \omega(\omega - m\Omega_H) \int_H dS \langle |\Psi|^2 \rangle, \quad (\text{A14})$$

and read off the superradiance condition

$$0 < \omega < m\Omega_H. \quad (\text{A15})$$

For the vector field, substituting (A5) into (A10), we have

$$\mathcal{F}^A = \int_H dS \langle \chi^\mu F_{\mu\alpha} t^\nu F_\nu{}^\alpha \rangle + \mu_V^2 \int_H d \langle \chi^\mu A_\mu t^\nu A_\nu \rangle, \quad (\text{A16})$$

where we have again used  $g_{\mu\nu} \chi^\mu t^\nu = 0$  on the horizon.

For the vector field, the mode decomposition is defined by

$$(\mathcal{L}_t A)_\mu = -i\omega A_\mu, \quad (\mathcal{L}_\chi A)_\mu = -i(\omega - m\Omega) A_\mu. \quad (\text{A17})$$

Now, noting

$$\chi^\mu F_{\mu\alpha} = \mathcal{L}_\chi A_\alpha - \nabla_\alpha (A_\mu \chi^\mu), \quad t^\nu F_{\nu\beta} = \mathcal{L}_t A_\beta - \nabla_\beta (A_\nu t^\nu), \quad (\text{A18})$$

and using Eq. (A17) and the Lorenz condition (14) we find

$$\chi^\mu F_{\mu\alpha} t^\nu F_\nu{}^\alpha = g^{\alpha\beta} \mathcal{L}_\chi A_\alpha \mathcal{L}_t A_\beta + \chi^\mu A_\mu \nabla^\alpha \nabla_\alpha (t^\nu A_\nu) + \text{divergence terms}. \quad (\text{A19})$$

On the horizon integral, we ignore the divergence terms and then obtain

$$\begin{aligned} \mathcal{F}^A &= \int_H dS \langle \text{Re}(\chi^\mu F_{\mu\alpha} t^\nu F_\nu{}^{\alpha*}) \rangle + \mu_V^2 \int_H dS \langle \text{Re}(\chi^\mu A_\mu t^\nu A_\nu^*) \rangle \\ &= \omega(\omega - m\Omega) \int_H dS \langle |A|^2 \rangle + \mu_V^2 \int_H dS \langle |\chi^\mu A_\mu t^\nu A_\nu| \rangle - \int_H dS \langle \text{Re}(\chi^\mu A_\mu \nabla^\alpha \nabla_\alpha (t^\nu A_\nu^*)) \rangle. \end{aligned} \quad (\text{A20})$$

If we impose

$$\chi^\mu A_\mu = 0 \text{ on } \mathcal{H}^+, \quad (\text{A21})$$

we get the simple formula, similar to the scalar field case (A14),

$$\mathcal{F}^A = \omega(\omega - m\Omega) \int_H dS \langle |A|^2 \rangle, \quad (\text{A22})$$

and the superradiance condition for the vector field is again given by (A15).

## Appendix B: Spin-weighted spherical harmonics

Here, we list the spin-weighted spherical harmonics up to  $l = 2$  in spherical coordinates  $\{\theta, \phi\}$  and Cartesian coordinates  $\{x, y, z\}$  given by Eq. (25). In case of spin-weight  $s = 0$  we obtain:

$l = 0$ :

$$Y_{00}^R = \frac{1}{\sqrt{4\pi}}, \quad Y_{00}^I = 0 \quad (\text{B1})$$

$l = 1$ :

$$Y_{10}^R = \sqrt{\frac{3}{4\pi}} \cos \theta = \sqrt{\frac{3}{4\pi}} \frac{z}{r}, \quad Y_{10}^I = 0, \quad (\text{B2a})$$

$$Y_{11}^R = -\sqrt{\frac{3}{8\pi}} \sin \theta \cos \phi = -\sqrt{\frac{3}{8\pi}} \frac{x}{r}, \quad Y_{11}^I = -\sqrt{\frac{3}{8\pi}} \sin \theta \sin \phi = -\sqrt{\frac{3}{8\pi}} \frac{y}{r}, \quad (\text{B2b})$$

$$Y_{1-1}^R = -Y_{11}^R, \quad Y_{1-1}^I = Y_{11}^I \quad (\text{B2c})$$

$l = 2$ :

$$Y_{20}^R = \sqrt{\frac{5}{16\pi}} (3 \cos^2 \theta - 1) = \sqrt{\frac{5}{16\pi}} \left( 3 \frac{z^2}{r^2} - 1 \right), \quad Y_{20}^I = 0, \quad (\text{B3a})$$

$$Y_{21}^R = -\sqrt{\frac{5}{8\pi}} \cos \theta \sin \theta \cos \phi = -\sqrt{\frac{5}{8\pi}} \frac{xz}{r^2}, \quad Y_{21}^I = -\sqrt{\frac{5}{8\pi}} \cos \theta \sin \theta \sin \phi = -\sqrt{\frac{5}{8\pi}} \frac{yz}{r^2}, \quad (\text{B3b})$$

$$Y_{22}^R = \sqrt{\frac{15}{32\pi}} \sin^2 \theta \cos(2\phi) = \sqrt{\frac{15}{32\pi}} \frac{x^2 - y^2}{r^2}, \quad Y_{22}^I = \sqrt{\frac{15}{32\pi}} \sin^2 \theta \sin(2\phi) = \sqrt{\frac{15}{8\pi}} \frac{xy}{r^2} \quad (\text{B3c})$$

$$Y_{2-1}^R = -Y_{21}^R, \quad Y_{2-1}^I = Y_{21}^I, \quad Y_{2-2}^R = Y_{22}^R, \quad Y_{2-2}^I = -Y_{22}^I \quad (\text{B3d})$$

where  $\cos(2\phi) = \cos^2 \phi - \sin^2 \phi$ ,  $\sin(2\phi) = 2 \cos \phi \sin \phi$ ,  $\cos(3\phi) = 4 \cos^3 \phi - 3 \cos \phi$  and  $\sin(3\phi) = 4 \cos^2 \phi \sin \phi - \sin \phi$ . We further summarize the  $s = -1$  spin-weighted spherical harmonics up to  $l = 2$ , where we have also defined  $\rho^2 = x^2 + y^2$ .

$l = 0$ :

$$_{-1}Y_{00}^R = 0, \quad _{-1}Y_{00}^I = 0 \quad (\text{B4})$$

$l = 1$ :

$$_{-1}Y_{1-1}^R = \sqrt{\frac{3}{16\pi}} \cos \phi (\cos \theta - 1) = \sqrt{\frac{3}{16\pi}} \frac{x(z-r)}{r\rho}, \quad (\text{B5a})$$

$$_{-1}Y_{1-1}^I = -\sqrt{\frac{3}{16\pi}} \sin \phi (\cos \theta - 1) = -\sqrt{\frac{3}{16\pi}} \frac{y(z-r)}{r\rho} \quad (\text{B5b})$$

$$_{-1}Y_{10}^R = -\sqrt{\frac{3}{8\pi}} \sin \theta = -\sqrt{\frac{3}{8\pi}} \frac{\rho}{r}, \quad _{-1}Y_{10}^I = 0 \quad (\text{B5c})$$

$$_{-1}Y_{11}^R = -\sqrt{\frac{3}{16\pi}} \cos \phi (1 + \cos \theta) = -\sqrt{\frac{3}{16\pi}} \frac{x(z+r)}{r\rho}, \quad (\text{B5d})$$

$$_{-1}Y_{11}^I = -\sqrt{\frac{3}{16\pi}} \sin \phi (1 + \cos \theta) = -\sqrt{\frac{3}{16\pi}} \frac{y(z+r)}{r\rho} \quad (\text{B5e})$$

$l = 2$ :

$$-{}_1Y_{2-2}^R = \sqrt{\frac{5}{16\pi}} \sin \theta (\cos \theta - 1) (2 \cos^2 \phi - 1) = \sqrt{\frac{5}{16\pi}} \frac{(z-r)(x^2-y^2)}{r^2 \rho}, \quad (\text{B6a})$$

$$-{}_1Y_{2-2}^I = -\sqrt{\frac{5}{4\pi}} \cos \phi \sin \phi \sin \theta (\cos \theta - 1) = -\sqrt{\frac{5}{4\pi}} \frac{xy(z-r)}{r^2 \rho} \quad (\text{B6b})$$

$$-{}_1Y_{2-1}^R = \sqrt{\frac{5}{16\pi}} \cos \phi (2 \cos^2 \theta - \cos \theta - 1) = \sqrt{\frac{5}{16\pi}} \frac{x(2z^2 - zr - r^2)}{r^2 \rho}, \quad (\text{B6c})$$

$$-{}_1Y_{2-1}^I = -\sqrt{\frac{5}{16\pi}} \sin \phi (2 \cos^2 \theta - \cos \theta - 1) = -\sqrt{\frac{5}{16\pi}} \frac{y(2z^2 - zr - r^2)}{r^2 \rho} \quad (\text{B6d})$$

$$-{}_1Y_{20}^R = -\sqrt{\frac{15}{8\pi}} \cos \theta \sin \theta = -\sqrt{\frac{15}{8\pi}} \frac{z\rho}{r^2}, \quad -{}_1Y_{20}^I = 0 \quad (\text{B6e})$$

$$-{}_1Y_{21}^R = -\sqrt{\frac{5}{16\pi}} \cos \phi (2 \cos^2 \theta + \cos \theta - 1) = -\sqrt{\frac{5}{16\pi}} \frac{x(2z^2 + zr - r^2)}{r^2 \rho}, \quad (\text{B6f})$$

$$-{}_1Y_{21}^I = -\sqrt{\frac{5}{16\pi}} \sin \phi (2 \cos^2 \theta + \cos \theta - 1) = -\sqrt{\frac{5}{16\pi}} \frac{y(2z^2 + zr - r^2)}{r^2 \rho} \quad (\text{B6g})$$

$$-{}_1Y_{22}^R = \sqrt{\frac{5}{16\pi}} \sin \theta (\cos \theta + 1) (2 \cos^2 \phi - 1) = \sqrt{\frac{5}{16\pi}} \frac{(z+r)(x^2-y^2)}{r^2 \rho}, \quad (\text{B6h})$$

$$-{}_1Y_{22}^I = \sqrt{\frac{5}{4\pi}} \cos \phi \sin \phi \sin \theta (\cos \theta + 1) = \sqrt{\frac{5}{4\pi}} \frac{xy(z+r)}{r^2 \rho} \quad (\text{B6i})$$

- [1] R. Ruffini, *Black Holes: les Astres Occlus* (Gordon and Breach Science Publishers, 1973).
- [2] V. Frolov (ed.) and I. Novikov (ed.), *Black hole physics: Basic concepts and new developments* (Kluwer Academic Publishers, 1989).
- [3] A. Arvanitaki, S. Dimopoulos, S. Dubovsky, N. Kaloper and J. March-Russell, Phys.Rev. **D81**, 123530 (2010), [0905.4720].
- [4] A. Arvanitaki and S. Dubovsky, Phys.Rev. **D83**, 044026 (2011), [1004.3558].
- [5] J. E. McClintock and R. A. Remillard, 0902.3488.
- [6] M. Heusler, Living Rev.Rel. **1**, 6 (1998).
- [7] P. T. Chrusciel, J. L. Costa and M. Heusler, Living Rev.Rel. **15**, 7 (2012), [1205.6112].
- [8] S. Hawking and W. Israel, (1979).
- [9] E. Berti, V. Cardoso and A. O. Starinets, Class.Quant.Grav. **26**, 163001 (2009), [0905.2975].
- [10] R. Konoplya and A. Zhidenko, Rev.Mod.Phys. **83**, 793 (2011), [1102.4014].
- [11] E. Berti, V. Cardoso and C. M. Will, Phys.Rev. **D73**, 064030 (2006), [gr-qc/0512160].
- [12] I. Kamaretsos, M. Hannam, S. Husa and B. Sathyaprakash, Phys.Rev. **D85**, 024018 (2012), [1107.0854].
- [13] R. H. Price, Phys.Rev. **D5**, 2419 (1972).
- [14] E. W. Leaver, Phys.Rev. **D34**, 384 (1986).
- [15] E. Ching, P. Leung, W. Suen and K. Young, Phys.Rev. **D52**, 2118 (1995), [gr-qc/9507035].
- [16] P. M. Morese and H. Feshbach, *Methods of Theoretical Physics, Part I* (Feshbach Publishing, Minneapolis, 1981).
- [17] V. Cardoso, S. Yoshida, O. J. Dias and J. P. Lemos, Phys.Rev. **D68**, 061503 (2003), [hep-th/0307122].
- [18] Y. B. Zel'dovich, Pis'ma Zh. Eksp. Teor. Fiz. **14**, 270 (1971).
- [19] Y. B. Zel'dovich, Zh. Eksp. Teor. Fiz. **62**, 2076 (1972).
- [20] J. Bekenstein, Phys.Rev. **D7**, 949 (1973).
- [21] V. Cardoso, S. Chakrabarti, P. Pani, E. Berti and L. Gualtieri, Phys.Rev.Lett. **107**, 241101 (2011), [1109.6021].
- [22] N. Yunes, P. Pani and V. Cardoso, Phys.Rev. **D85**, 102003 (2012), [1112.3351].
- [23] V. Cardoso and P. Pani, 1205.3184.
- [24] P. Hut, Astrono. Astrophys. **99**, 126 (1981).
- [25] F. Verbunt, The earth and moon: from halley to lunar ranging and shells, <http://www.astro.uu.nl/~verbunt/onderwijs/binary/earth.pdf>.
- [26] W. H. Press and S. A. Teukolsky, Nature **238**, 211 (1972).
- [27] V. Cardoso, O. J. Dias, J. P. Lemos and S. Yoshida, Phys.Rev. **D70**, 044039 (2004), [hep-th/0404096].
- [28] V. Cardoso and O. J. Dias, Phys.Rev. **D70**, 084011 (2004), [hep-th/0405006].
- [29] V. Cardoso, O. J. Dias and S. Yoshida, Phys.Rev. **D74**, 044008 (2006), [hep-th/0607162].
- [30] H. Kodama, Prog.Theor.Phys.Suppl. **172**, 11 (2008), [0711.4184].
- [31] N. Uchikata, S. Yoshida and T. Futamase, Phys.Rev. **D80**, 084020 (2009).

- [32] T. Damour, N. Deruelle and R. Ruffini, *Lett.Nuovo Cim.* **15**, 257 (1976).
- [33] T. Zouros and D. Eardley, *Annals Phys.* **118**, 139 (1979).
- [34] S. L. Detweiler, *Phys.Rev.* **D22**, 2323 (1980).
- [35] H. Furuhashi and Y. Nambu, *Prog.Theor.Phys.* **112**, 983 (2004), [gr-qc/0402037].
- [36] V. Cardoso and S. Yoshida, *JHEP* **0507**, 009 (2005), [hep-th/0502206].
- [37] S. R. Dolan, *Phys.Rev.* **D76**, 084001 (2007), [0705.2880].
- [38] S. Hod, *Physics Letters B* 708, **320-323** (2012), [1205.1872].
- [39] S. Hod, *Phys.Rev.* **D86**, 104026 (2012), [1211.3202].
- [40] P. Pani, V. Cardoso, L. Gualtieri, E. Berti and A. Ishibashi, *Phys.Rev.Lett.* **109**, 131102 (2012), [1209.0465].
- [41] P. Pani, V. Cardoso, L. Gualtieri, E. Berti and A. Ishibashi, *Phys.Rev.* **D86**, 104017 (2012), [1209.0773].
- [42] J. G. Rosa and S. R. Dolan, *Phys.Rev.* **D85**, 044043 (2012), [1110.4494].
- [43] H. Kodama and H. Yoshino, *Int.J.Mod.Phys.Conf.Ser.* **7**, 84 (2012), [1108.1365].
- [44] H. Yoshino and H. Kodama, *Prog.Theor.Phys.* **128**, 153 (2012), [1203.5070].
- [45] G. Mocanu and D. Grumiller, *Phys.Rev.* **D85**, 105022 (2012), [1203.4681].
- [46] J. G. Rosa, 1209.4211.
- [47] C. Herdeiro, M. O. Sampaio and M. Wang, *Phys.Rev.* **D85**, 024005 (2012), [1110.2485].
- [48] M. Wang, M. O. Sampaio and C. Herdeiro, 1212.2197.
- [49] M. Khlopov, B. Malomed and I. Zeldovich, *Mon.Not.Roy.Astron.Soc.* **215**, 575 (1985).
- [50] M. Y. Khlopov, *Res.Astron.Astrophys.* **10**, 495 (2010), [0801.0116].
- [51] J. Barranco *et al.*, *Phys.Rev.* **D84**, 083008 (2011), [1108.0931].
- [52] J. Barranco *et al.*, *Phys.Rev.Lett.* **109**, 081102 (2012), [1207.2153].
- [53] J. Alsing, E. Berti, C. M. Will and H. Zaslauer, *Phys.Rev.* **D85**, 064041 (2012), [1112.4903].
- [54] M. Goodsell, J. Jaeckel, J. Redondo and A. Ringwald, *JHEP* **0911**, 027 (2009), [0909.0515].
- [55] J. Jaeckel and A. Ringwald, *Ann.Rev.Nucl.Part.Sci.* **60**, 405 (2010), [1002.0329].
- [56] P. G. Camara, L. E. Ibanez and F. Marchesano, *JHEP* **1109**, 110 (2011), [1106.0060].
- [57] A. S. Goldhaber and M. M. Nieto, *Rev.Mod.Phys.* **82**, 939 (2010), [0809.1003].
- [58] J. Rosa, *JHEP* **1006**, 015 (2010), [0912.1780].
- [59] S. Hod, *Phys.Rev.* **D84**, 044046 (2011), [1109.4080].
- [60] M. J. Strafuss and G. Khanna, *Phys.Rev.* **D71**, 024034 (2005), [gr-qc/0412023].
- [61] S. R. Dolan, 1212.1477.
- [62] A. B. Balakin and W.-T. Ni, *Class.Quant.Grav.* **27**, 055003 (2010), [0911.2946].
- [63] M. Alcubierre, *Introduction to 3+1 numerical relativity* International series of monographs on physics (Oxford Univ. Press, Oxford, 2008).
- [64] C. M. Chambers and I. G. Moss, *Class.Quant.Grav.* **11**, 1035 (1994), [gr-qc/9404015].
- [65] M. Giammatteo and I. G. Moss, *Class.Quant.Grav.* **22**, 1803 (2005), [gr-qc/0502046].
- [66] R. Konoplya and A. Zhidenko, *Phys.Rev.* **D73**, 124040 (2006), [gr-qc/0605013].
- [67] E. Berti, V. Cardoso and M. Casals, *Phys.Rev.* **D73**, 024013 (2006), [gr-qc/0511111].
- [68] E. Newman and R. Penrose, *J.Math.Phys.* **3**, 566 (1962).
- [69] C. Palenzuela, L. Lehner and S. Yoshida, *Phys.Rev.* **D81**, 084007 (2010), [0911.3889].
- [70] P. Mosta *et al.*, *Phys.Rev.* **D81**, 064017 (2010), [0912.2330].
- [71] M. Zilhao, V. Cardoso, C. Herdeiro, L. Lehner and U. Sperhake, *Phys. Rev. D* **85**, 124062 (2012), arXiv:1205.1063 [gr-qc].
- [72] U. Sperhake, *Phys.Rev.* **D76**, 104015 (2007), [gr-qc/0606079].
- [73] T. Goodale *et al.*, The Cactus framework and toolkit: Design and applications, in *Vector and Parallel Processing – VECPAR’2002, 5th International Conference, Lecture Notes in Computer Science*, Berlin, 2003, Springer.
- [74] Cactus Computational Toolkit, <http://www.cactuscode.org/>.
- [75] E. Schnetter, S. H. Hawley and I. Hawke, *Class.Quant.Grav.* **21**, 1465 (2004), [gr-qc/0310042].
- [76] Mesh refinement with Carpet, <http://www.carpetcode.org/>.
- [77] D. Shoemaker *et al.*, *Class.Quant.Grav.* **20**, 3729 (2003), [gr-qc/0301111].
- [78] U. Sperhake, B. J. Kelly, P. Laguna, K. L. Smith and E. Schnetter, *Phys.Rev.* **D71**, 124042 (2005), [gr-qc/0503071].
- [79] A. Zenginoglu, G. Khanna and L. M. Burko, 1208.5839.
- [80] S. Hod and T. Piran, *Phys.Rev.* **D58**, 044018 (1998), [gr-qc/9801059].
- [81] H. Koyama and A. Tomimatsu, *Phys.Rev.* **D64**, 044014 (2001), [gr-qc/0103086].
- [82] H. Koyama and A. Tomimatsu, *Phys.Rev.* **D65**, 084031 (2002), [gr-qc/0112075].
- [83] L. M. Burko and G. Khanna, *Phys.Rev.* **D70**, 044018 (2004), [gr-qc/0403018].
- [84] T. Damour, N. Deruelle and R. Ruffini, *Nuovo Cimento Lettere* **15**, 257 (1976).
- [85] Gravity group CENTRA/IST Lisbon, <http://blackholes.ist.utl.pt/?page=Files>.
- [86] N. Andersson, *Phys.Rev.* **D51**, 353 (1995).
- [87] E. Berti and V. Cardoso, *Phys.Rev.* **D74**, 104020 (2006), [gr-qc/0605118].
- [88] V. Cardoso, <http://gamow.ist.utl.pt/~vitor/?page=ringdown>.
- [89] C. Vishveshwara, *Nature* **227**, 936 (1970).
- [90] R. Konoplya and C. Molina, *Phys.Rev.* **D75**, 084004 (2007), [gr-qc/0602047].